Physics – Uspekhi **64** (3) 253 – 279 (2021)

REVIEWS OF TOPICAL PROBLEMS

PACS numbers: **61.46.–w**, 62.20.Qp, **62.25.–g**, 68.35.Gy

Protective coatings with nanoscale multilayer architecture: current state and main trends

A D Pogrebnjak, M A Lisovenko, A Turlybekuly, V V Buranich

DOI: https://doi.org/10.3367/UFNe.2020.08.038823

Contents

Abstract. **Binary systems (layers) and multicomponent layers with bilayer thicknesses varying from microns to a few nanometers are considered. A strong dependence of the microstructure formation on the deposition conditions (the magnitude of the bias potential, the flow of inert and reactive gases, the ion beam power (current density) supplied to the target) is found. General regularities in the change in the functional properties and structural state of the coatings are formulated. The conditions for the formation of a columnar structure and growth texture are noted; various mechanisms and their interpretation are proposed. The relationship among the size of nanograins, diffusion at the interphase boundary, and effects determining the physico-mechanical, tribological characteristics, as well as resistance to corrosion and oxidation, is shown.**

Keywords: multilayer coatings, nanocomposites, structure, hardness, wear, corrosion

A D Pogrebnjak [1,2,a], **M A Lisovenko** [1,3],
A Turlybekuly [2,4], **V V Buranich** [1,b].
[1] Sumy State University,
Rymskogo-Korsakova 2, 40007 Sumy, Ukraine
[2] Al-Farabi Kazakh National University,
Al-Farabi Ave. 71, 050040 Almaty, Republic of Kazakhstan
[3] Materials Science Division, Argonne National Laboratory,
9700 South Cass Ave., Argonne, Illinois, 60439, USA
[4] Nazarbaev University,
Kabanbay Batyr Ave. 53, 010000 Nur-Sultan,
Republic of Kazakhstan
E-mail: [a] alexp@i.ua, [b] v.buranich@phe.sumdu.edu.ua

Received 23 January 2020, revised 13 July 2020
Uspekhi Fizicheskikh Nauk **191** (3) 262 – 291 (2021)
Translated by V L Derbov

1. Introduction

Today, upgrading by deposition of coatings based on transition metal nitrides and intermetallic compounds is a promising way to improve the performance of industrial products. The option to transform such protective coatings into a nanostructured state has been proposed, as has the formation of multilayer structures with nanoscale architecture [1–5]. The gradient character of multilayer structures allows implementing multiple functions, such as enhancing adhesion and improving wear and corrosion resistance. Alternating two or more layers of materials with different physical-mechanical characteristics makes it possible to change the properties of the system, including those of stress concentrators, to affect the propagation of cracks by increasing the material fracture toughness [6–15]. Of particular interest are multilayer compositions based on binary nitrides TiN/CrN, TiN/MoN, ZrN/CrN, ZrN/MoN, and ZrN/AlN.

In the literature, hypotheses from various fields of the natural sciences are commonly used, namely, solid state physics, physical materials science, chemical physics, and condensed matter physics. Multilayer nanocomposite coatings are of particular interest, since they possess some special physical, chemical, and micromechanical properties, such as high-temperature stability [14], hardness, and improved heat-protecting properties that are the most suitable for operation under extreme tribological conditions [16–23].

2. Structure and properties of multilayer binary coatings

2.1 Effect of nanograin size and interfaces on the characteristics of coatings

Developing new technical solutions in the cutting tool industry and modernizing processing steps with an increased load level, e.g., in the automobile and aircraft industries, require advancing new multifunctional materials capable of providing improved mechanical, tribological, and high-temperature properties. Three stages of the coating formation process can be distinguished: initial grain formation, the growth of amorphous clusters, and ultimately joining them into an intercrystalline phase (the final stage) [24]. This process depends on many parameters, which substantially complicates the prognosis of the structure and phase composition of materials, although offering new opportunities of producing coatings with unique properties.

An important role in the formation of nanostructured films and coatings is played by the control of crystallographic orientation and size of grains via changing the particle energy in the course of deposition and mass transfer, implanting individual elements in a solid composite matrix, or varying the layers of nanoscale thickness with an alternation of amorphous and crystalline phases. In this case, the film microstructure is substantially affected by the substrate temperature and the energy of ions that transfer their kinetic energy to the coating in the course of deposition [15, 25–27]. Such specificity is mainly characteristic of the magnetron sputtering method, in which the energy of deposited particles depends on the working gas pressure in the vacuum chamber, the distance from the source to the substrate, and the magnitude of the bias potential applied to the substrate.

Vacuum-arc deposition is a highly ionizing technology that uses an ion energy of the order of 10 eV, which allows regulating the zonal temperature and kinetics of interaction with the cathode spot from which the ions and neutral particles participating in the coating formation are emitted. Therefore, the structure and substructure substantially depend on energy of particle collisions, and, by changing the pool of parameters, one can set the preferable range of the physical-mechanical properties of coatings [18, 26, 28].

The main criteria for obtaining desirable properties of nanocrystalline films are the grain size and crystallographic orientation, which is ensured by ion bombardment during deposition. The efficiency of ion bombardment manifests itself in a reduction in crystallite size, the relaxation of compressing stresses, the compaction of grain boundaries, and localization of radiation defects, which leads to changes in the coating properties [28–33]. In this case, the optimal method to control the size of crystallites in the direction of the coating growth is the formation of a multilayer architecture with nanoscale layers. Such a structure of the coating is produced by periodic deposition of thin layers of different compounds with a given thickness.

Reference [34] presents a classification of solid-state coatings by their bond type (Fig. 1). Nitrides, carbides, and carbonitrides of transition metals (especially elements in groups IV B, V B, and VI B of the periodic system) are among the most suitable materials for creating wear-resistant coatings.

The structure and composition distribution in a multilayer coating relative to individual layers, interphase boundaries, and their dimensional ratios allows setting the functionality of a modernized surface by controlling its properties, such as hardness, strength, and elasticity.

The deposition of a multilayer structure is accompanied by an increase in the proportion of phase-separating boundaries relative to the total amount of interfaces, which impedes the propagation of dislocations and cracks, thus enhancing the mechanical resistance of the system. However, the decrease in the thickness of the obtained layers is limited by extreme values, upon reaching which the interphase boundaries become diffuse [35–37]. Therefore, studies of the phase state, structure, and physical-mechanical properties of these nanoscale complexes are of particular scientific and practical interest.

According to the inverse Hall–Petch effect [38], maximal hardness values are achieved in nanocrystalline materials with a grain size of the order of 10 nm. The grain-size hardening occurs at the expense of intercrystallite processes, such as absorption of a dislocation core by an interface and interaction with point defects [9, 39, 40].

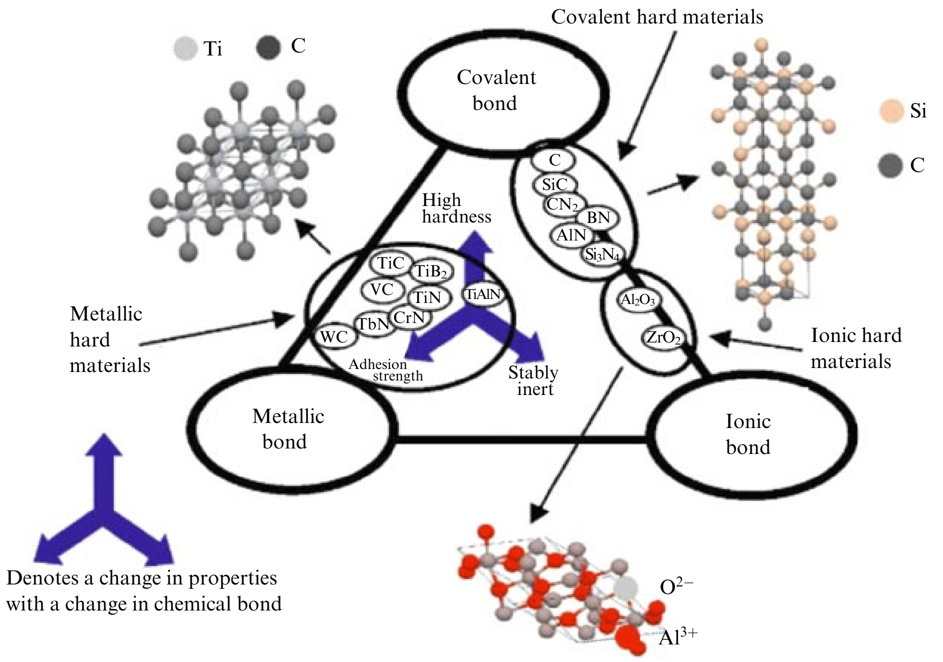

Figure 1. Classification of groups of hard coatings by bonding type and crystal structure [34].

In References [15, 24, 41, 42], the effect of grain size and near-surface effects at the film-substrate interfaces on the strengthening mechanisms was studied. A strong dependence of the coating structure and properties on the technological parameters of its production is also manifested, which complicates unambiguous interpretation of the nature of the structures grown. At phase-to-phase boundaries, the atoms of crystal lattices of different thin layers in multilayer films can substitute each other, giving rise, in turn, to additional energy of deformation proportional to the shear modulus of the material. Layers with different shear moduli impede the motion of dislocations. Moreover, the trajectory deviations or redistributions of dislocations and cracks at the grain boundaries increase the resistance of coatings to destruction. Periodic alternation of nanoscale layers with different physical-mechanical characteristics allows a substantial change in the properties of multilayer architecture, like the concentration of internal stresses, the propagation of cracks, and, hence, an increased fracture toughness (crack resistance) of the structure [30, 43].

The first results of the deposition of hard and super-hard structures based on multicomponent and multilayer coatings and a description of appropriate formation mechanisms appeared as early as the mid-1980s [44–46], so that to date there have been a great number of both theoretical and experimental studies on the development of multilayer coatings. As a rule, the hardening mechanisms are divided into (1) compressing macrostresses arising in the coating during its growth, (2) plastic deformation caused by dislocation motion, (3) the effect of nanograin size, (4) solid solution formation, and (5) the manifestation of cohesion forces between the atoms of adjacent grains [47]. At the same time, the superhardness (beyond 40 GPa) of nanostructured multilayer coatings requires a high coherence between the layers and a grain size close to critical. Therefore, the geometry, thickness, and order of layers greatly influence this seemingly ambiguous effect [3, 48].

Proceeding from the preliminary results obtained for multilayer coatings, it is possible to present a simplified model as a sequential alternation of several layers of single-phase materials with an optimal individual layer thickness of 10 to 100 nm. It was soon recognized that a limit reduction in both the layer thickness and the crystallite size (to a few nanometers) leads to a substantial change in the coating properties. Therefore, besides the layer composition, the chemical bonds formed at the interfaces are of extreme importance. In Ref. [49], the distribution of the structural properties of earlier obtained hard and superhard multilayer physical vapor deposition (PVD) coatings depending on the amount of interphase boundaries is studied. It should be noted that the optimal protective properties of such coatings can be achieved only under definite volumes of interphase boundaries (the ratio of interface width to the total film thickness).

To describe the structural interaction in the given heterostructures, the bilayer modulation period can be distinguished as a specific parameter. Optimal properties are manifested at a period of 50–100 nm. This fact opens a new direction in nanostructure design: the coating properties directly depend on interactions at interphase boundaries.

The issue of the existing mechanisms and their modified options is worth particular attention. In the course of studies, a series of experimental investigations of mechanical, elastic, and plastic properties of multilayer systems via the examples of crack formation and propagation and energy dissipation were performed [34, 50, 51].

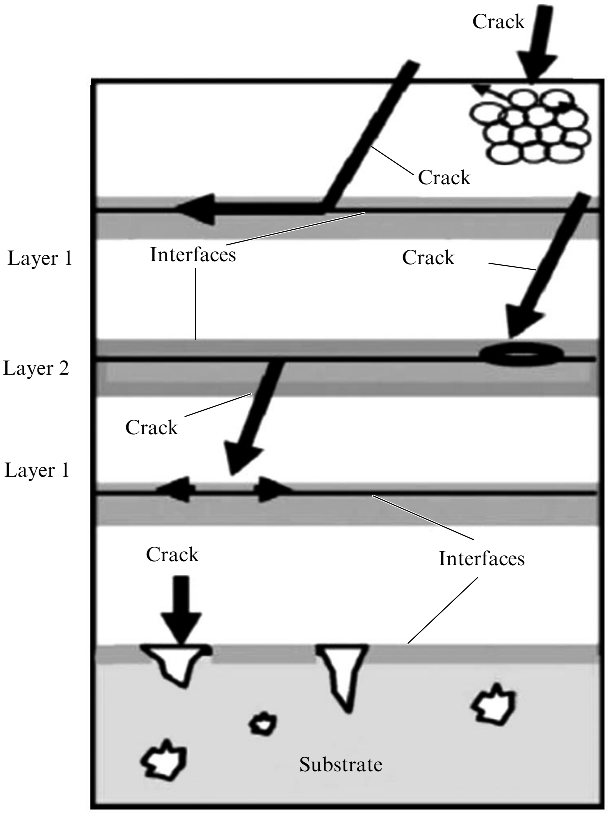

Figure 2. Conventional mechanism of crack propagation in multilayer systems and crack distribution at interphase boundaries [34].

Mechanical loads produce multiple actions on a multilayer structure, which comprise surface effects (cracking) and the deformation of inner layers of interphase boundaries, as well as changes at the grain boundaries and the response of the entire coating. A crack begins on the surface and can then branch and change its trajectory at the grain boundaries (grain boundary strengthening); similar processes also occur at the interfaces between layers (phase boundary strengthening). On the other hand, a local delamination can take place at the interfaces due to the presence of nanoscale cavities, which leads to the local relaxation of internal stresses and increases the plasticity at a nanoscale level. Moreover, there is interaction of cracks with periodic deformations at interphase boundaries in nanoscale multilayer structures, as well as interaction of penetrating cracks with the substrate material. These mechanisms are schematically illustrated in Fig. 2 [34].

From the point of view of dislocation motion, due to the presence of multiple grain boundaries in a nanocomposite coating, the dislocations propagating through grains begin to slow down their motion at the grain boundaries, which leads to their accumulation. Therefore, their further movement requires an increased stress, which is exactly why the hardness increases [26, 52]. The density of dislocations grows with the decrease in the grain size; hence, the hardness also increases proportionally to the nanograin size. However, it is extremely important that at very small grain sizes (less than 2–3 nm) no universal mechanism of dislocation accumulation be admissible, since dislocations cannot be generated in small grains. It is accepted that sliding along grain boundaries and migration

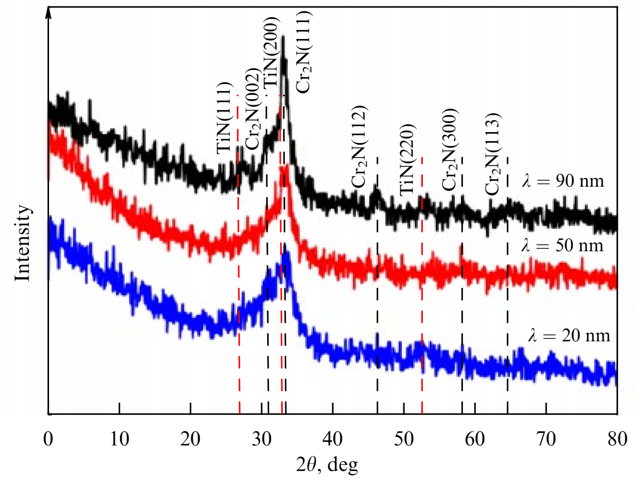

Figure 3. Diffraction patterns of TiN/CrN coatings with different bilayer periods [53].

of grains play an important role in reducing the hardness at small grain sizes, which is better known as the inverse Hall–Petch effect [38].

Internal interphase boundaries demonstrate a positive effect on micro-and macroscopic properties of the entire coating if their amount is carefully chosen relative to the total coating volume.

The influence of such parameters as grain size, periodicity, and the structure of interphase boundaries on the microstructure of multilayer coatings can be considered using the example of the TiN/CrN system [53]. By means of radio-frequency (RF) magnetron sputtering in argon, three series of multilayer samples of TiN/CrN on a silicon substrate with a bilayer thickness of $\lambda = 20$, 50, and 90 nm were obtained. The thickness of the samples was 916, 707, and 880 nm, the roughness and grain size slightly differing from sample to sample. As is known, the higher the energy of sputtered particles, the more easily Ar atoms and ions migrate on the substrate surface. Moreover, due to the combination of sputtering energy and ion mass in the process of island growth, the grain size in each sublayer increases with film thickness. Therefore, if the modulation period amounts to 50 nm, a region of increased grain size appears on the film surface (transition from 114 to 126 nm).

Figure 3 shows X-ray photographs of TiN/CrN multilayer films with a bilayer period of 20, 50, and 90 nm. The TiN/CrN films are seen to contain a mixture of TiN and Cr_2N phases. It was found that all TiN and CrN microstructures in the TiN/CrN system, independent of the bilayer period, are single-phase face-centered cubic (fcc) lattices. The intensity of the (200) peak is more expressed for TiN, while the growth direction (111) corresponds to the CrN phase. A nanostructure study of the multilayer TiN/CrN coating using transmission electron microscopy (TEM) in the cross section and the corresponding selected area electron diffraction (SAED) patterns are shown in Fig. 4. The layers of TiN and CrN are alternatingly arranged along the growth direction. Dark layers with a mean thickness of 12, 35, and 60 nm are CrN, and light layers with a mean thickness of 8, 15, and 30 nm correspond to TiN. It is definitely established that the interface width gradually decreases with an increase in the bilayer period. The SAED images incorporate both broken and continuous ring lines, which correspond to a superposition of individual TiN (111) and (200) and CrN (100), (110), (111), (210), and (112) diffraction patterns, which also confirms the crystallographic orientations obtained from X-ray diffraction (XRD) spectra. In the case of TiN/CrN, a strong dependence of the microstructure on the layer periodicity is observed. The results obtained in Ref. [53] are correlate well with similar studies of binary systems [4, 54, 55]. In this case, microscopic mechanisms that largely affect the process of interface growth were not completely determined.

Measurements of nanohardness by the indentor penetration depth showed that multilayer coatings with a small periodicity possess higher hardness values (22, 26, and 28 GPa) than single-layer ones. The hardness tends to increase with a decrease in the modulation period, which correlates with the results obtained by other research teams [56–58]. As a rule, the grain boundaries impede the propagation of cracks; therefore, multilayer coatings possess better

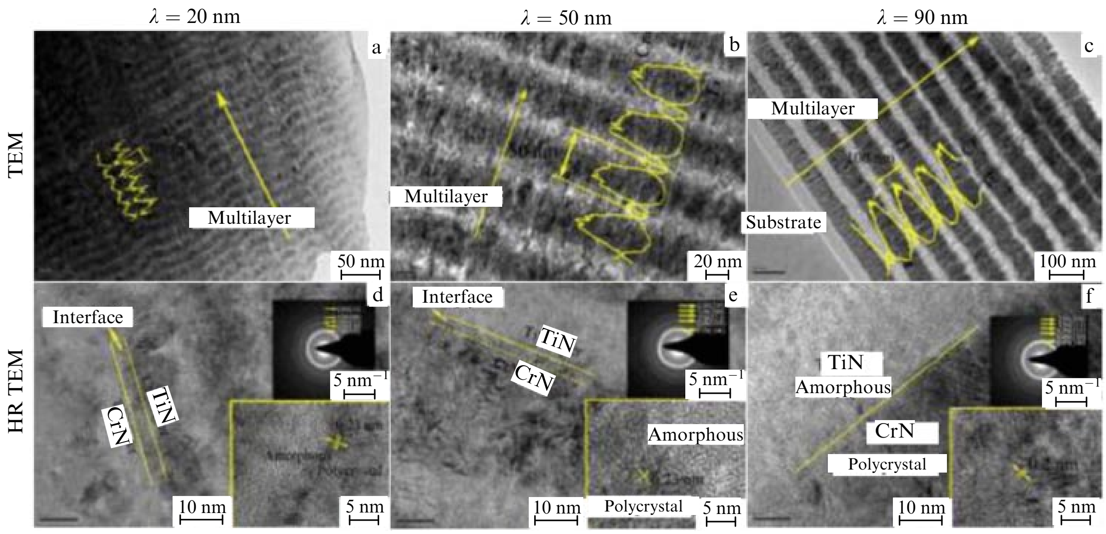

Figure 4. (a–c) TEM and high-angle annular dark-field (HAADF) microscopy images of the cross section of multilayer TiN/CrN films; (d–f) images of interface in a TiN/CrN multilayer film, obtained using HR-TEM and SAED [53].

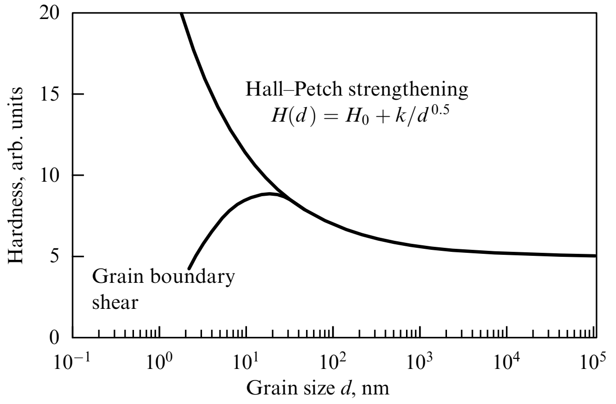

Figure 5. Illustrative behavior of hardness (Hall–Petch law) for polycrystalline films depending on the grain size [3].

hardness than single-layer ones because of increased interfaces. In the deposited multilayer coatings, the hardness increases with a decrease in the bilayer thickness.

From the TEM studies, it can be seen how the hardness is related to the specific contribution of interphase boundaries. According to the Hall–Petch dimension law, the yield stress in polycrystals increases with a decrease in the grain size (Fig. 5). The hardness of thin films depends on the grain size according to the formula

$$H = H_0 + kd^{-1/2}\,, \tag{1}$$

where H is the hardness of polycrystalline materials with grain size d, H_0 is the hardness of the same materials with large grains, and k is an empirical constant. The Hall–Petch model implies that dislocations cannot cross the grain boundary but can be collected at the grain boundary and create a new source of dislocations at the adjacent boundary. Such blocking of dislocations is more greatly expressed at mixed interphase boundaries. In addition, a particular composite structure, in which the amorphous and polycrystalline phases alternate, will generate an alternating strain field due to the lattice mismatch between the layers. The fluctuating stress field will decrease the growth of cracks, but this effect is considered small compared to the energy effects of the dislocation line [59, 60].

Besides the grain geometry, the physical-mechanical properties are greatly affected by the grain crystallographic orientation. In the case of single-layer coating deposition, the grain orientation is largely determined by the substrate material and orientation [3, 11, 61]. In nanocomposite structures, an increased interphase region is present, which makes the contribution of surface and interphase energy dominant. This enhances the hardness, strength, and wear resistance as compared to single-layer analogs [62]. By manipulating the ratio of layer thickness and grain size, a trend to a change in the surface energy can be revealed; therefore, a transition to one preferable orientation or another is possible. In this case, the first (template) layer will determine the orientation of the subsequent layers recrystallized in the process of layer growth. Thus, for example, in Ref. [63], devoted to NbN/MoN nanocomposites, the crystallographic orientation changed from (111) to (200) with a lower surface energy, as the thickness of the template layer of molybdenum exceeded 2.1 nm. In Ref. [64], it was revealed that in TiN/Si_3N_4 coatings the structure changed from (111) to randomly-oriented when the grain size decreased from 50 to 20 nm or less, which allowed regulation of wear resistance and hardness of the obtained coatings.

As shown in Fig. 6a, multilayer coatings possess lower values of residual stress than single-layer ones. The residual stress in multilayer TiN/CrN films with a periodicity of 20 nm is compressive or tensile, the contribution of the latter gradually increasing with a bilayer thickness increase. Figures 6b–d show the distribution of residual stresses measured by an electron tester. The integral residual stress of the film is minimal at a bilayer thickness of 20 nm, and the residual stress distribution in this case is maximally uniform. However, the general trend is that the greater the modulation period, the more inhomogeneous the residual stress distribution. Considering the microstructure observed using TEM, we see that the corresponding interphase boundaries can weaken the formation of stresses.

The calculated values of coating plasticity are presented in Fig. 6a. It is seen that multilayer coatings have a higher plasticity than single-layer ones. A single-layer TiN coating is harder than a CrN one, but its plasticity is lower than that of CrN. The fracture toughness K_{IC} is known to increase with the growth of plastic resistance [65]. Thus, an increase in fracture toughness decreases the film hardness. In multilayer TiN/CrN structures, the higher the compression stress, the

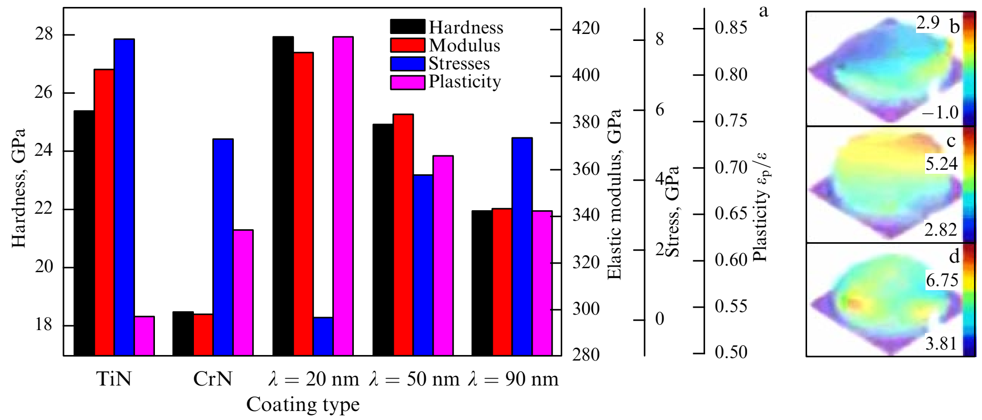

Figure 6. (Color online.) (a) Comparative diagram of mechanical properties of single-layer TiN , CrN, and multilayer TiN/CrN films. Three-dimensional distribution of residual stresses for multilayer TiN/CrN films with a modulation period of 20 nm (b), 50 nm (c), and 90 nm (d) [53].

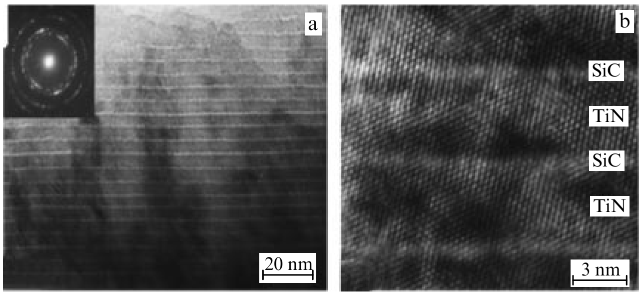

Figure 7. High-resolution TEM images of a multilayer TiN/SiC sample cross section with layer thickness of 0.6 nm (SiC) and 4.3 nm (TiN) with small (a) and large (b) magnification [6].

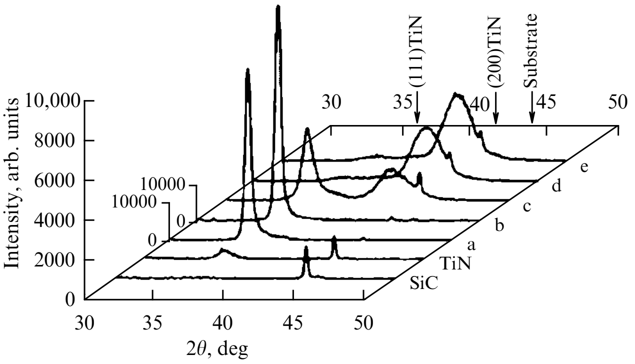

Figure 8. X-ray diffraction patterns of multilayer TiN/SiC films with different thicknesses of SiC layers (TiN thickness is equal to 4.3 nm): $l_{\mathrm{SiC}} = 0.4$ nm (a), 0.6 nm (b), 0.8 nm (c), 1.6 nm (d), and 2.4 nm (e) [6].

higher the plasticity and fracture toughness. The hardness and elastic modulus of multilayer films gradually increase with a decrease in the residual stress. This circumstance testifies to the fact that the compression stress effectively improves the fracture toughness. However, the impact toughness rapidly decreases with an increase in the tensile stress. As a result of such a process, tensile stresses can considerably worsen the fracture toughness of the film. The tensile stress will stimulate crack initiation and growth, whereas the residual compression stress at the top of a crack can facilitate crack occlusion. When a crack propagates, the tensile stress causing the initiation and growth of the crack should overcome the compression stress in the film, consuming additional energy. Meanwhile, a decrease in periodicity positively affects both the hardness and the impact toughness.

The next stage of investigations implies a transition to the finer nanoarchitecture of composite layers [6, 33, 66, 67]. Nanoscale single-layer TiN and SiC films, as well as multilayer TiN/SiC films, were fabricated using HF-magnetron sputtering. In Ref. [6], two series of multilayer samples with a total thickness of about 2 mm were considered. For the first series, the thickness of a single TiN layer amounted to 4.3 nm and the thickness of an SiC layer varied from 0.4 to 2.4 nm. For the second series, the SiC thickness was maintained at a level of 0.6 nm, while the TiN thickness varied from 2.5 to 19.8 nm.

Preliminary consideration of single-layer and multilayer films using energy-dispersive X-ray spectroscopy (EDS) showed that both TiN and SiC have a stoichiometric structure. The high-resolution TEM (HR TEM) image of the cross section presented in Fig. 7 demonstrates a distinctly modulated composition structure consisting of TiN (dark layers) and SiC (light layers). It was found that the SiC layers with a thickness up to 0.6 nm are homogeneous, with planar grains and a very narrow mixing region. A SAED analysis of the chosen region confirms the formation of a polycrystalline fcc structure. The TiN structure in this case is presented in the form of a cubic B1 lattice (with a tabular value of B1 lattice constant $a_{\mathrm{TiN}} = 4.249$ Å), whereas for B1-SiC the value is $a_{\mathrm{SiC}} = 4.3596$ Å. An image of the same sample with increased resolution (Fig. 7b) showed that the SiC layers were completely crystallized and grown epitaxially with the TiN layers.

Small-angle X-ray diffraction peaks of superlattices (Fig. 8) also indicate the presence of a multilayer structure, except in the first sample with the SiC layer thickness of 0.4 nm. Based on the position of the superlattice peaks, the modulation periods were calculated using the modified Bragg law [68]. The X-ray patterns in Fig. 8 testify to the amorphous character of a single-layer SiC film. The broad and less expressed (111) peak for the TiN film shows that under the chosen conditions of deposition extremely small crystals of TiN formed. However, in multilayer materials with a very thin layer of SiC (0.4–0.6 nm), intense diffraction (111) peaks of TiN are observed. Worth noting is the mixing of TiN layers, which changes the growth regime at the interfaces and leads to a smoother morphology.

On the other hand, an X-ray diffraction analysis (see Fig. 8) of multilayer films with a constant thickness of SiC ($l_{\mathrm{SiC}} = 0.6$ nm) and varied TiN thicknesses showed that the TiN (111) diffraction peaks in these films have a close intensity, although the peaks corresponding to the TiN thickness of 9.5 and 19.8 nm are somewhat broadened. Obviously, the change in the TiN thickness had a minor effect on the condition of the SiC layers and the corresponding epitaxially grown structure.

The curves of Vickers hardness (HV) versus the thickness of SiC and TiN layers are shown in Fig. 9. From the presented plots, it is seen that the coating hardness greatly depends on the nanomodulation of the layers. When the SiC thickness increases to 0.6 nm, the film hardness is doubled to 60.6 GPa, but with a further increase in layer thickness the hardness decreases to nearly 30 GPa. The anomalous increase in hardness (superhardness) is due to a number of factors, such as the difference in share moduli (dislocation line energy) of layers, a layer thickness (0.6 nm) sufficiently small for dislocation movement in several layers, and maximal matching of the layers. A further increase in the SiC thickness leads to damage of the coherent boundaries and the formation of amorphous domains, which undoubtedly decreases the hardness.

When the TiN layer thickness was changed from 2.5 to 19.8 nm, all multilayer samples demonstrated a significant increase in hardness, from 40 GPa, which is twice that in a TiN coating obtained under the same conditions. Such evolution of microstructure in multilayer systems can be explained considering thermodynamic and kinetic factors that affect the film growth and microstructure [6, 25]. A microstructure analysis revealed that multilayer films with SiC layer thickness $l_{\mathrm{SiC}} = 0.6$ nm meet all the above requirements and, therefore, demonstrate extremely high hardness. A further increase in the SiC layer thickness violates the interface coherence because of amorphous SiC layer formation, so that a decrease in the hardness of the multilayer system is observed. Vice versa, if the SiC layers are too thin ($l_{\mathrm{SiC}} < 0.4$ nm), then the continuous growth of the system is impeded, and the hardness increase is minor.

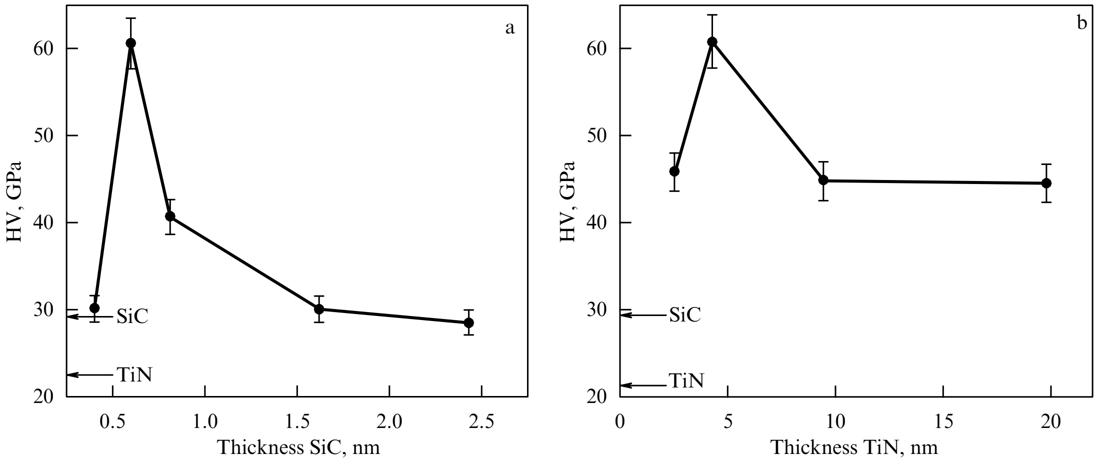

Figure 9. Curves of Vickers hardness of multilayer films versus layer thickness l_{SiC} (at $l_{\mathrm{TiN}} = 4.3$ nm) and l_{TiN} (at $l_{\mathrm{SiC}} = 0.6$ nm) [6].

Within the framework of thermodynamic theory, the formation of a metastable structure is described assuming no possibility of forming a coherent interface, when two materials with different crystal structures are deposited in a multilayer structure, as in the case of TiN/AlN [69]. The diffusion of adatoms against the growth background is well known to be the most important kinetic process of film growth [70, 71]. If the diffusion mobility is sufficient, a greater number of adatoms will overcome the potential energy barrier and travel from metastable domains to stable ones. Therefore, in the process of film deposition, the formation of perfect crystals will become more probable. The authors of [6] supposed that the inhomogeneous growth in multilayer structures is energetically preferable for adatom diffusion; hence, SiC has a tendency to grow in an ordered crystalline form. Increasing the mobility of the deposited TiN particles leads to higher crystallicity of all elements of a multilayer structure. However, the effect of heterogeneous surfaces can spread over a limited range, which in the present study was shown to vanish under an increase in SiC thickness to 0.8 nm. The amorphous layers of SiC, in turn, affect the TiN growth, blocking the epitaxial growth of the multilayer system.

As a result, a few approaches can be proposed to explain the mechanisms of the superhardness phenomenon, including dislocation blocking at the interfaces, the different natures of internal strain in individual layers, and the enhancement of the inverse Hall–Petch effect. All the considered models have mutual prerequisites for achieving superhardness. First, two composite layers must have different shear moduli and, therefore, different dislocation line energies. Second, all layers must be sufficiently thin to restrict the formation and movement of dislocations in individual layers. Finally, and most importantly, two levels of modulation must form matched interfaces [72–74]. If a multilayer coating satisfies these criteria, significant internal stress providing dislocation transfer along an interface is necessary to increase the hardness.

2.2 Change in potential and energy of the incident particles of ion-plasma flow

The substrate bias voltage and the working pressure are very important deposition parameters affecting the kinetic energy of ions. One of the ways to represent the ion energy is the following formula [75]:

$$E = \frac{KV_{\mathrm{b}}}{Pm}\,, \quad 0 \leqslant m \leqslant 1\,, \tag{2}$$

where K is a constant, V_{b} is the bias voltage at the substrate, P is the working pressure, and m is a coefficient. It is seen that the kinetic energy of ions is proportional to the bias voltage if the working pressure and other parameters of deposition are unchanged. When the sputtered ions arrive on the film surface, the bombarding ions create a few vacancies in the film. The kinetic energy of the interacting ions increases and facilitates the filling of pores and voids in the film, particularly at the positions of vacancies, with an increase in the substrate bias potential. Thus, the remaining vacancies of the last bombarding ions are partially filled by the newly sputtered ions, which leads to greater compaction of the film.

The effect of repeated sputtering of arriving ions also enhances when the substrate bias voltage is increased. Meanwhile, the accompanying increase in adatom mobility, also affected by the target composition (light and heavy element) and the deposition parameters (e.g., the range of working pressures), can be considered the main contribution of the bias potential [72, 76]. The mobility of adatoms is related to the residual energy after growth, as well as the substrate temperature and the nature of the growth. Therefore, similar to the substrate temperature affecting the integrity of film crystals, the growth conditions play an important role in the process of phase structure and composition formation. Thus, it is possible to assert that the coating growth texture, particularly with a complex architecture, will not simply change proportionally to the potential change, but also greatly depends on the above parameters [77], such as the deposition rate [11–13, 15].

In Ref. [76], multilayer nanoscale coatings of CrN/NbN and TiN/WN with a modulation period from 3 to 3.5 nm were considered. The texture coefficient was calculated for them, and the influence of the bias potential during the deposition was estimated.

Figure 10 illustrates the effect of the bias potential V_{b} on the texture development of the nanoscale multilayer CrN/NbN and TiN/WN coatings. The coatings consist of relatively heavy elements (the atomic number is greater than 52) and form layers with the growth texture in the direction (100). In the case of heavy atoms Nb and W, they are relatively immobile even at the bias voltages $V_b = -120$ V. Thus, the immobile layers of Nb and W atoms in layers with a high content of WN and NbN interrupt the columnar growth, causing repeated grain formation, so that the texture is formed in the same way as in the case of thin film deposition, when the surface energy is dominant and facilitates the development of the {100} texture.

This type of growth is characteristic of single-layer multicomponent films, e.g., TiAlCrYN [78, 79], which form the {100} texture when there is less than 5 at.% of heavy elements with lower mobility in the elemental composition. Under the same conditions of the deposition of a TiAlCrN coating without the heavy Y, the texture {111} is formed, developing in the process of competitive growth. Increasing the bias potential on the substrate to −150 V stimulates the mobility of all atoms and, therefore, decreases the interruption of the columnar growth, leading to the formation of a mixed {111} and {100} texture in CrN/NbN films deposited at $V_b = -150$ V.

All the studied coatings demonstrate insignificant compressive residual stresses. It is commonly accepted that higher residual stresses are related to a higher density of defects caused by ion bombardment. In the deposited coatings, the prevailing contribution to high-energy bombardment is made by Ar^+ ions. Two particular processes in the course of ion bombardment are the transfer of kinetic energy to the sputtered particles and the formation of defects during the growth of the coating [80, 81]. One of the possible explanations for systematically lower residual stress is that the activation energy spent on the surface diffusion of heavy and less mobile atoms Nb and W is greater than that for lighter atoms (Ti and Cr).

In coatings based on heavy metal compounds, with energy conservation during the deposition at fixed bias voltage taken into account, a smaller part of the total energy is available for defect formation, since the greater part is spent to move the atoms to the equilibrium positions. In this case, a smaller residual stress will be created in the coating [76, 87, 88]. An example of this effect is seen in the samples of CrN/NbN and TiN/WN nanostructure coatings presented in Fig. 10, where the maximum stress obtained for the coating deposited at $V_b = -75$ V is only 1.8 GPa, further increase in the bias voltage to −150 V for the multilayer CrN/NbN coating leads to an increase in the residual stress to 6.8 GPa. At the same time, the residual stress for the TiN/WN coating with a heavier element W in its matrix increased to 4 GPa at $V_b = -120$ V.

On the other hand, the change in the negative bias potential affects the atomic concentration of the reactive gas, as a rule, nitrogen. In the course of studies of the CrN/MoN multilayer structure [82] with gradation of the modulation period, three series of samples were considered with different negative bias potentials during the deposition. The first discovered phenomenon was that at high bias potentials the atomic ratio N/(Cr + Mo) in the layers changes from 0.3 to 0.5 due to the transformation of vacant sites as a result of selective sputtering during ion bombardment.

In the course of X-ray diffraction analysis for the first series of samples ($V_b = -20$ V), the growth of crystals with the [311] (Fig. 11) axis was revealed to be preferable, which manifests itself in the relative enhancement of the corresponding reflex. In CrN layers, such a texture is more expressed. Increasing the bias potential to $V_b = -150$ V facilitated the formation of another type of texture, {111}, which improved with the growth of layer thickness; however, at large diffraction angles, it is possible to observe the formation of a solid solution.

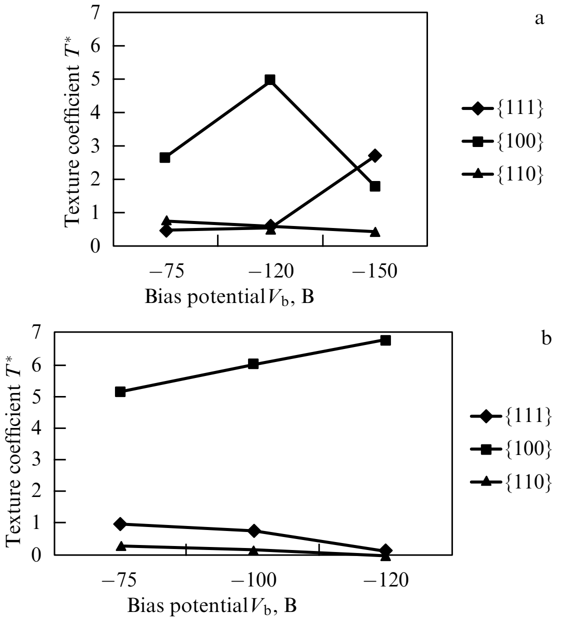

Figure 10. Influence of the bias potential on texture development in multilayer coatings (a) CrN/NbN and (b) TiN/WN [76].

Upon a further increase in the applied potential to $V_b = -300$ V (see Fig. 11), the texture growth substantially changes in the direction [200]. Thus, an evolution of preferable texture growth from [311] to [111] and then to [200] is observed, when the negative bias voltage applied to the substrate changes from −20 to −150 and −300 V, respectively. This can be associated with insignificant changes in the nitrogen concentration, with the growth of ion energy due to selective secondary sputtering and repeated deposition [82, 89–91].

The second parameter that also affects the energy condition of the deposition process is the working pressure. Reference [82] shows that a decrease in nitrogen pressure P_N from 0.4 to 0.09 Pa leads to the formation of hexagonal phase β-Cr_2N and FCC phase γ-Mo_2N. The growth direction corresponds to the peaks (110), (002) for β-Cr_2N and (111), (200) for γ-Mo_2N. Such a texture evolution in CrN/MoN films with a decrease in the nitrogen pressure is shown in Fig. 11d. At $P_N = 0.09$ Pa, when the bias potential increases to −150 V, the predominant growth of crystallites occurs in the directions [002] and [200] for the phases β-Cr_2N and γ-Mo_2N, which increases the mismatch between the structures of the layers.

For coatings of the 2nd and 3rd series deposited at $V_b = -150$ V or −300 V, the size of crystallites calculated using the Scherrer equation [92] decreases to 2 nm, when the bilayer thickness reaches nanoscale values; in this case, the order of crystallite microstrains amounts to 0.4–0.5%. These values are relatively higher in the coatings of the first series deposited at $V_b = -20$ V, where the microstrain is 1.5% for CrN and 2.3% for γ-Mo_2N, which can be explained by the lower mobility of the deposited atoms, leading to a smaller probability of diffusion healing of growth defects. The crystallite size for the coating of the first series decreases

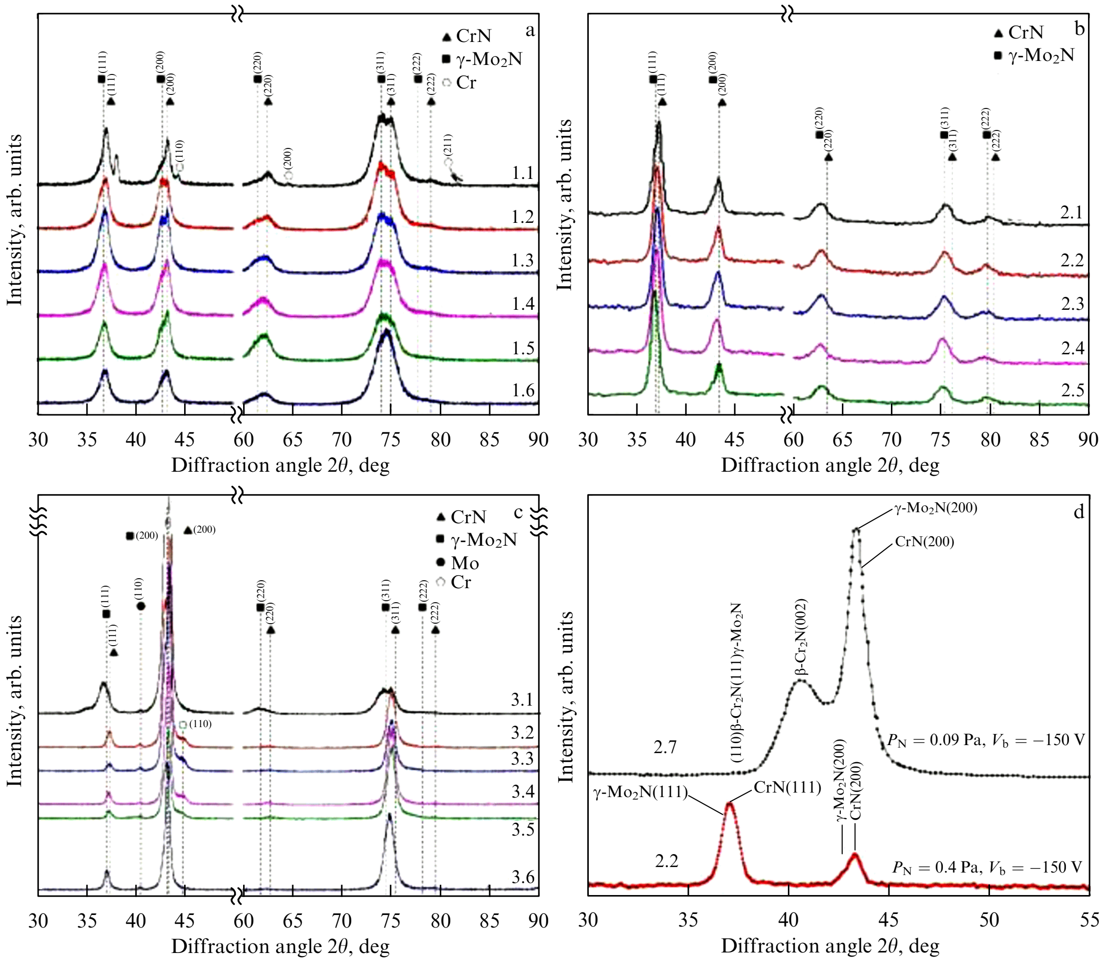

Figure 11. X-ray diffraction patterns of CrN/MoN multilayer coatings: spectra of samples deposited at a negative bias voltage of −20 V (a), −150 V (b), and −300 V (c), and a comparison of samples deposited at different nitrogen pressures (d) [82].

from 17.2 nm (for CrN) and 11.5 nm (for γ-Mo_2N) to 8.3 and 5.8 nm, respectively, at the bilayer thickness of 44 nm. The calculated residual stresses in samples of the 1st and 2nd series were 5.3 GPa for CrN and 6.9 GPa for γ-Mo_2N.

It should be noted that for other nanoscale multilayer heterostructures, TiN/SiN, ZrN/SiN, and TiN/AlN, manifesting the superhardness effect [52, 93–96], it was found that a thin interphase layer of B1-SiN and B1-AlN is formed near the layers of TiN and ZrN. Note that TiN/SiC heterostructures and chemical relations in a carbide-nitride compound were less studied. A few research teams obtained nanoscale multilayer films of TiN/SiC [6, 97]. It was shown that the epitaxial interphase layers of B1-SiC (*Fm*3*m*-216) formed between the layers of TiN at an SiC layer thickness of less than 0.6–0.8 nm. Thus, SiC crystallization and epitaxial growth between the layers of TiN and SiC ensure a high hardness of the order of 60 GPa. The authors of Ref. [6] presented the dependence of Vickers hardness HV on the thickness of TiN layers that varied from 2.5 to 19.8 nm, while the SiC thickness was fixed at 0.6 nm. The coating hardness was about 40 GPa for various thicknesses of TiN layers (from 9.5 to 19.8 nm), and the nanohardness attained values of about 18 GPa. The dependence of the universal hardness (HU) on the indentor penetration depth is observed when the SiC thickness varies from 0.4 to 2.4 nm, and the thickness of TiN layers remains unchanged. Theoretical studies of the TiN (001) heterostructure and B1-SiC monolayer confirmed the thermal stability up to 600 K [98], whereas at the interface the B1-SiC structure transformed into the structure B3-SiC even under low-temperature conditions.

In the subsequent experimental and theoretical study [7], nanoscale multilayer TiN/SiC films were obtained by magnetron sputtering of TiN and SiC targets at different substrate temperatures T_S = 25, 100, 200, and 350 °C; single-layer TiN and SiC films 700 nm thick obtained at T_S = 350 °C were also considered.

Grazing incidence X-ray diffraction (GI-XRD) patterns of multilayer TiN/SiC films deposited at different substrate temperatures are shown in Fig. 12 in comparison with that of a single-layer TiN film. A weak peak at angles $2\theta = 36.5°$ in multilayer films obtained at substrate temperatures of 25 and 100 °C corresponds to small TiN crystallites that actively form with the increase in the substrate temperature. In these films, there are no crystallites corresponding to silicon carbide. It can be hypothesized that low-temperature films are sequences of nanocrystalline layers of TiN with tiny grains separated by amorphous layers of SiC. Note that high-temperature nanolayer films deposited at T_S = 200 and 350 °C consist of larger TiN grains.

Diffraction patterns of multilayer films obtained at a substrate temperature of 350 °C exhibit insignificant peaks at $2\theta = 35.6°$, 40.5°, 41.5°, and 65.8°, related to small-size crystallites of hexagonal and cubic silicon carbide (3C-SiC) and demonstrate weak (001) textures. It can be supposed that

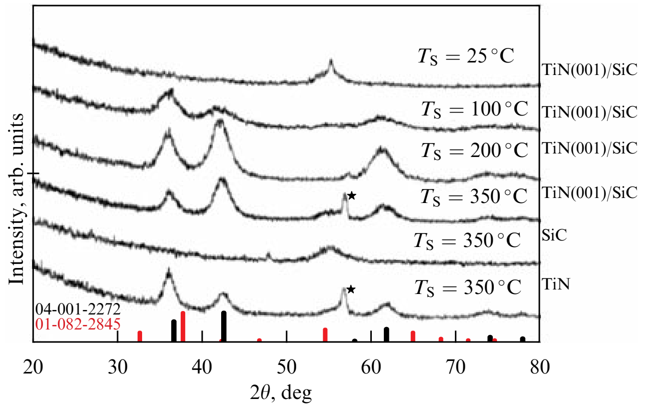

Figure 12. (Color online.) GI-XRD diffraction patterns of multilayer TiN/SiC films and single layers of SiC and TiN deposited at different substrate temperatures T_S. The red vertical lines correspond to SiC, black lines to TiN; the stars label the hexagonal phase [7].

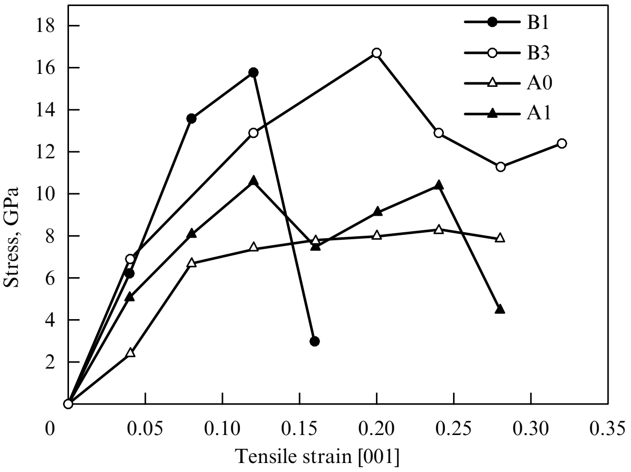

Figure 13. Stress vs tensile strain curves for TiN(001)/SiC heterostructures generated in different atomic configurations of TiN(001)/SiC [7].

films produced under high-temperature conditions (200–350 °C) are nanocrystalline (nc) multilayer systems of the nc-TiN/nc-SiC type. This allows a conclusion that the substrate temperature of 350 °C under the experimental conditions of the considered work is the threshold temperature at which the layers of amorphous SiC begin to crystallize. It should be noted that SiC single-layer films deposited at $T_S = 350$ °C are highly amorphous; therefore, the layers of SiC in multilayer compounds crystallize due to the crystal structure of TiN layers.

Also worthy of interest are studies of heterostructure behavior under tension. The ideal tensile strength (σ_T, the maximal stress achieved under tension) values of B1, B3, and A1 heterostructures and A0 amorphous structure are 16, 17, 11, and 8 GPa, respectively. Keeping this fact in mind, it is possible to suppose that the three-layer 3C-SiC structure will be the most stable one of all those considered. The most unstable structure is A0 (amorphous a-SiC). Thus, the formation of amorphous interfaces in TiN(001)/SiC heterostructures will worsen their mechanical characteristics. It is important that all interfaces in TiN(001)/SiC heterostructures experience similar structural transformations after fracture [6, 8, 98]. All heterostructures (except B3) break down because of separation of the TiN and SiC layers. In the case of the B3 heterostructure, the interphase boundaries are so strong that the fracture occurs in the layer of TiN (Fig. 13).

Calculations of TiN(001)/SiC heterostructures obtained under different deposition conditions showed that the B1-SiC interface is sufficiently stable and can arise between TiN layers at low temperatures. However, with increasing temperature the boundaries become unstable because of lattice expansion. According to theoretical results, the thinner the interphase B1-SiC layer in the TiN(001)/SiC heterostructure, the higher its strength, but to achieve the maximum strength, the B3-SiC structure should consist of several SiC layers.

The obtained results allow formulating the basic conditions for enhancing the strength of nanolayer TiN/SiC films. In particular, they should be deposited at low or moderate temperatures to ensure the formation of heteroepitaxial cubic or hexagonal SiC interfaces that comprise more than one SiC monolayer. In this case, the ultimate SiC layer thickness should be selected equal to 3 nm, below which the deposition of films at low temperatures ensures the formation of heteroepitaxial B1-SiC layer [7, 98].

2.3 Proceeding from micron to nanoscale bilayer thickness

In studies of coatings with a multilayer architecture, the main role is played by the bilayer thickness (modulation period) of the chosen system. The periodicity and the effect of multiple layers facilitate the improvement of the coating quality, since at interphase boundaries the formation of new compounds, partitioning, and the redistribution of defects in the process of deposition occur. This concept was described in the previous sections of the present review. A factor of particular importance for the efficiency of interfaces is their specific volume relative to the coating total thickness, as well as relative to the thickness of individual layers [73, 99, 100].

Let us consider the results of recent studies of nanostructured ZrN/CrN coatings using the physical methods of deposition of bilayers with thicknesses from 2.2 to 300 nm, published by various authors. The results clearly demonstrate that the hardness, elastic modulus, and other physical-mechanical and tribological properties of coatings are affected by a variety of factors, first and foremost, the conditions of coating deposition [27].

The high homogeneity and columnar structure of ZrN/CrN coatings are shown in Fig. 14. It is clearly seen that the coating repeats the relief of the substrate surface. The coating structure is dense and the boundary between the coating and the substrate is distinctly expressed, which is supposed to facilitate adhesion between the coating and the substrate. It should be noted that the layered structure of coatings can remain continuous over a few millimeters [101–103], which exceeds their extremely small thickness (1–10 nm) by many orders of magnitude.

The coatings obtained by vacuum arc deposition can have various phase and defect structures. In this case, the grain structure is presented by columnar crystals directed from a transition layer to the coating surface vertically or at a certain angle [32, 104, 105].

Atomic force microscopy images of the coating surfaces are shown in Fig. 15. The images testify to the fact that, depending on the bilayer thickness, the mean roughness varies from 1.9 to 4.4 nm. The relief nonuniformity can be explained by the presence of macrodefects on the surface, as well as the specificity of reactive sputtering in an atmosphere of light nitrogen atoms. Studies have shown that a coating

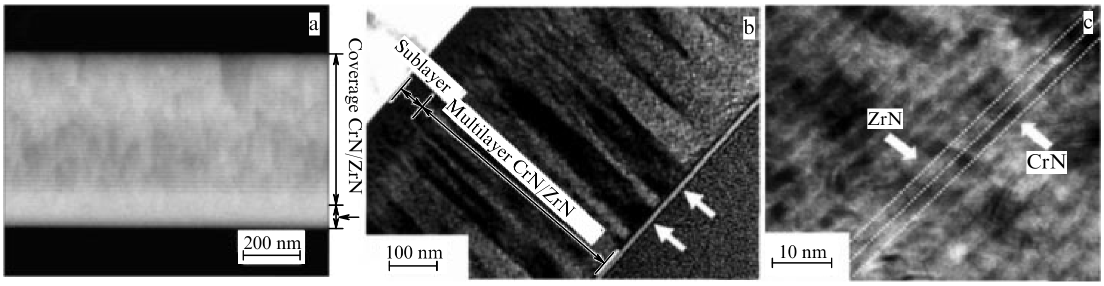

Figure 14. (a) Electron microscopy images of side surface of ZrN/CrN multilayer coatings with layer thickness of 16 nm [83]. TEM images of the cross section of multilayer ZrN/CrN system with a modulation period of 5 nm, obtained with low (b) and high (c) resolution [84].

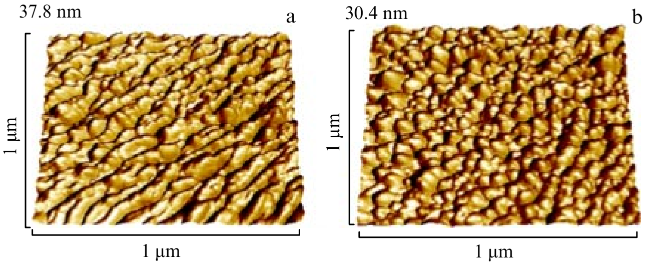

Figure 15. Images of parts of a surface obtained using an atomic force microscope for ZrN/CrN coatings with a bilayer thickness of 3 μm (a) and 375 nm (b) [85] (the mean roughness is indicated above the images).

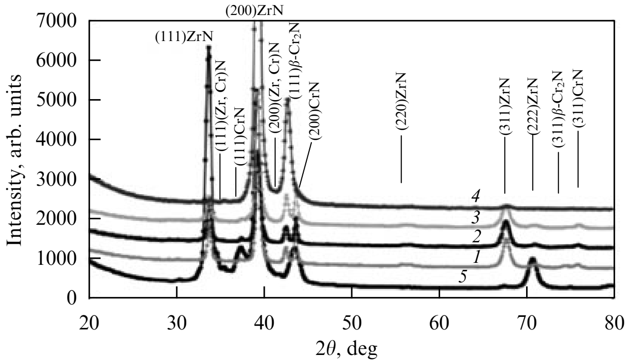

Figure 16. Areas of diffraction spectra of multilayer ZrN/CrN films obtained with different values of layer thickness: *1* — 300 nm; *2* — 120 nm; *3* — 80 nm; *4* — 40 nm; *5* — 20 nm [67].

with a bilayer thickness of 100 nm has the minimum roughness (1.9 nm), and a coating with a thickness of 375 nm has the minimum grain size (39 nm).

X-ray diffraction studies of multilayer ZrN/CrN coatings yield close results in a number of papers [84, 106, 107]. As the bilayer thickness decreases, the CrN reflexes permanently shift towards smaller angles (Fig. 16). The ZrN diffraction maximum is practically unchanged with a decrease in bilayer thickness to 35 nm. Upon a further decrease in the modulation period, a substantial broadening of the peak and its displacement towards greater diffraction angles are observed. Such a shift can be related to a decrease in the grain size and degree of crystallinity. When the bilayer thickness reaches 11.7 nm, the X-ray diffraction pattern exhibits a predominant growth of the CrN phase with a (111) reflex, i.e., as the bilayer thickness decreases, the multilayer structure transforms into a 'superlattice structure' with one lattice parameter. This is seen from the presence of a single peak with satellites in the X-ray diffraction pattern. The peak corresponds to an interplanar spacing of $d = 2.45$ Å, which is median between the interplanar spacing d_{111} of zirconium nitride and d_{111} of chromium nitride.

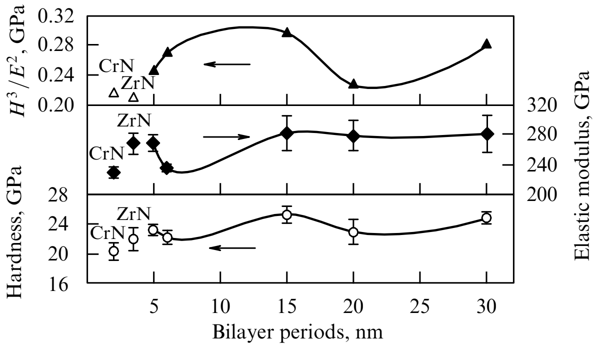

Figure 17. Hardness, elasticity modulus, and deformation depending on the value of the bilayer period in CrN/ZrN multilayer coatings [84].

Something similar has already been observed in multilayer systems and is promising for application in multilayer structures with superthin layers [108, 109]. In a number of papers [27, 84], it was shown that layers of chromium nitride can be formed at different proportions of the CrN and Cr_2N phases. The two-phase composition of this kind is due to the use of pulsed high-voltage applied to the substrate during the vacuum arc process of coating formation. In this case, the applied DC negative potential varies from −70 to −150 V. According to additional studies [107], the formation of the Cr_2N phase may be caused by the mixture of the reaction gas, in this case $N_2 + NH_3$. The flow velocity of the reaction gas also affects the coating stoichiometry. The working pressure in the chamber is about 0.28 Pa. Parts of diffraction spectra of such coatings are shown in Fig. 16. Summarizing the presented data, we can say that the main parameter that determines the appearance or absence of the Cr_2N phase is not so much the partial pressure of the reaction gas as the energy contribution that depends on the value of the supplied bias potential, as well as the working gas pressure. With the above results taken into account, it is worth noting the extremely strong dependence of the film formation structure and kinetics on the technological parameters of the film formation process.

To illustrate the effect of bilayer thickness on mechanical characteristics, Figs 17, 18 present appropriate dependences of the hardness H, elastic modulus E, and deformation H^3/E^2 for the ZrN/CrN [84] and TiN/WN [86] systems. It is possible to trace a certain tendency to the optimization of physical-mechanical properties in the considered range of modulation period values. Depending on the composition of the layers, the optimum can vary; for particular cases, we have 10.2 nm for TiN/WN and 16 nm for ZrN/CrN.

Table 1. Deposition conditions and characteristics of ZrN/CrN coatings [27].

Material	Fabrication method	Deposition parameters	Characteristics		References
			Tribological	Mechanical	
ZrN/CrN	Vacuum arc deposition	Substrate: Si and TiC $\lambda = 16$ nm $l = 565-577$ μm $I = 70$ A $P_{\mathrm{N}} = 8.6 \times 10^{-1}$ Torr $V_{\mathrm{b}} = -100$ V $T_{\mathrm{s}} = 150\,^{\circ}\mathrm{C}$	$\mu = 0.41-0.45$, $w = 3.62 \times 10^{-7}-$ 4.26×10^{-4} mm^3 N^{-1} m^{-1}, $K_{\mathrm{IC}} = 1.85-2.01$ MPa m$^{1/2}$	$H = 28$ GPa $E = 267$ GPa $H^3/E^2 = 0.11$ GPa	[83]
ZrN/CrN	Vacuum arc deposition	Substrate: Si and TiC $\lambda = 5-30$ nm $l = 511-677$ μm $d = 2.9-4.69$ nm $I = 70$ A $P_{\mathrm{N}} = 8.6 \times 10^{-1}$ Torr $V_{\mathrm{b}} = -100$ V $T_{\mathrm{s}} = 150\,^{\circ}\mathrm{C}$	$\mu = 0.17-0.05$ $w = 3.62 \times 10^{-7}-$ 4.26×10^{-4} mm^3 N^{-1} m^{-1} $K_{\mathrm{IC}} = 1.88-2.15$ MPa m$^{1/2}$	$H = 25.2$ GPa $E = 282$ GPa $H^3/E^2 = 0.3$ GPa	[84]
ZrN/CrN	Magnetron sputtering	Substrate: Si, steel AISI M2 $\lambda = 11.7-66.7$ nm $l = 1.9-2.1$ μm $P_{\mathrm{N}} = 5 \times 10^{-4}$ Pa $V_{\mathrm{b}} = -60$ V $N = 30-180$	$\mu = 0.32-0.54$ $w = 5.5 \times 10^{-7}$ mm^3 N^{-1} m^{-1}	$H = 29$ GPa $E = 256$ GPa	[110]
ZrN/CrN	Magnetron sputtering	Substrate: steel AISI 420 $\lambda = 100-1000$ nm $l = 3$ μm $d = 39-99$ nm $P_{\mathrm{N}} = 6.6 \times 10^{-3}$ mbar $V_{\mathrm{b}} = -60$ V $T_{\mathrm{s}} = 250\,^{\circ}\mathrm{C}$ $N = 1, 8, 15, 30$	$\mu = 0.32-0.54$		[85]
ZrN/CrN	Magnetron sputtering	Substrate: steel AISI H13 $\lambda = 2.1-7.1$ nm $d = 6.2-9.4$ nm $P_{\mathrm{N}} = 3.3 \times 10^{-3}$ Torr $V_{\mathrm{b}} = -100$ V $T_{\mathrm{s}} = 150\,^{\circ}\mathrm{C}$ $v_{\mathrm{s}} = 3, 6, 15$ rpm^{-1}	$w = 0.74 \times 10^{-6}$ mm^3 N^{-1} m^{-1}	$H = 28.1-31.8$ GPa $E = 290-321$ GPa $H^3/E^2 = 0.19-0.31$ GPa	[106]
ZrN/CrN	Magnetron sputtering	Substrate: Si $\lambda = 2.2-3.6$ nm $l = 1-1.2$ μm $P_{\mathrm{N}} = 0.26$ Pa $V_{\mathrm{b}} = -200$ V $T_{\mathrm{s}} = 250\,^{\circ}\mathrm{C}$ $v_{\mathrm{s}} = 4-11$ rpm^{-1}	Breaking load 85 mN $w = 0.38 \times 10^{-5}$ mm^3 N^{-1} m^{-1}	$H = 32$ GPa	[111]
ZrN/CrN	High-current magnetron sputtering	Substrate: Si $l = 800-1000$ nm $P_{\mathrm{N}} = 0.28$ Pa $V_{\mathrm{b}} = -200$ V $T_{\mathrm{s}} = 200\,^{\circ}\mathrm{C}$ $v_{\mathrm{s}} = 13$ rpm^{-1}	Breaking load 100 mN	$H = 48.39-56.47$ GPa $E = 381$ GPa	[107]
ZrN/CrN	Vacuum arc deposition	Substrate: steel AISI 321 $\lambda = 90-732$ nm $l = 16$ μm $P_{\mathrm{N}} = 0.16-0.2$ Pa $V_{\mathrm{b}} = -150$ V $T_{\mathrm{s}} = 250\,^{\circ}\mathrm{C}$		$H = 22.3-24.6$ GPa $E = 295-318$ GPa	[112]
ZrN/CrN	Vacuum arc deposition	Substrate: steel AISI 321 $\lambda = 359-140$ nm $l = 11.1-15.3$ μm $P_{\mathrm{N}} = 0.08-0.43$ Pa $V_{\mathrm{b}} =$ with -70 to -150 V $T_{\mathrm{s}} = 250\,^{\circ}\mathrm{C}$		$\mathrm{HV}_{0.025} =$ $2795-4685$ GPa	[113]

Notation in the table: P_{N} — nitrogen pressure, V_{b} — bias voltage, T_{s} — substrate temperature, I — cathode current, v_{s} — velocity of substrate rotation, l — film thickness, λ — period, d — grain size, N — number of layers, H — hardness, μ — friction coefficient, w — wear rate, K_{IC} — fracture toughness, E — elasticity modulus, H^3/E^2 — deformation, HV — Vickers hardness.

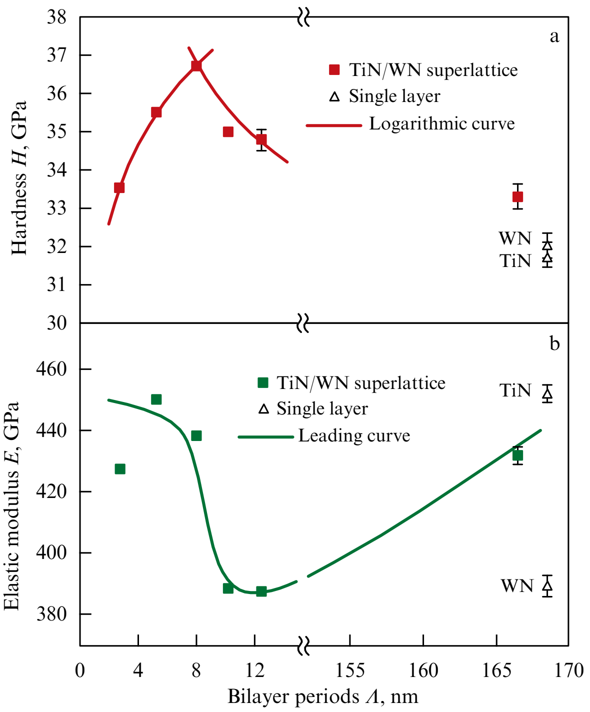

Figure 18. Plots of hardness (a) and elasticity modulus (b) vs bilayer period for TiN/WN superlattices [86].

3. Effect of bilayer elemental composition on the characteristics of coatings

3.1 Changing the energy parameters of vacuum arc and magnetron discharge

The process of film formation begins from a substrate surface that is impacted by a flow of deposited atoms. The coating material is adsorbed and an equilibrium state established: a chemical bond with the substrate atoms is formed. On completion of nucleation, the uniform growth of clusters or islets is provided by the activation energy of the deposited material and the substrate, as well as by adatom mobility, which is also fully affected by the parameters of the sputtering process [114, 115]. Materials with low activation energy rapidly condense and, as a rule, form amorphous films; this frequently occurs in materials with a nonmetallic type of bonding. Since the temperatures of the substrate and the deposited atoms are different, partial supersaturation and surface diffusion occur. The character of the transition from the moment of nucleation completion to the beginning of grain growth remains unclear [116, 117]; however, in [118, 119], some approaches and models have already been developed.

Depending on the difference between the strength of adatom–substrate and adatom–adatom bonds, various mechanisms of growth can take place [120]. If the atoms are strongly bonded, 3D island-like (nucleation) Volmer–Weber growth occurs. In this case, small stable clusters appear, which join into islets and accrete onto a continuous film. Such a mechanism is characteristic of metallic films. If, on the contrary, the bonding of the sputtered atoms with the substrate is stronger than between the atoms, a 2D layer-by-layer (Frank–van der Merwe) growth occurs, which is typically observed in metal–metal and semiconductor–semiconductor systems. A third type of growth, layer-plus-island (Stranski–Krastanov), is a combination of the first two. In this case, due to a release of elastic energy accumulated in the film, the coherence of the film-substrate interface is violated, decreasing the bonding energy. Thus, the interphase energy determines the formation of a thin intermediate layer of an island. This type of growth is characteristic of metal–metal and metal–semiconductor systems.

The coating growth kinetics during the sputtering substantially depend on such parameters as the deposition time, substrate temperature, and pressure in the chamber. These parameters directly regulate the formation and growth of defects, their coalescence, and processes related to recrystallization. On the other hand, the bias potential on the substrate is one of the most important controlled parameters of deposition, which affects the mobility of adatoms during coating deposition/growth. Therefore, the study of the bias voltage role in the formation of structural defects is of particular scientific interest, since various defects considerably worsen the coating properties. For example, metallic inclusions can increase the wear rate by worsening the structure homogeneity and creating uncontrollable interfaces with the initiation of internal defects [121–123]. Incomplete coatings with the presence of such defects as pores, cracks, and cavities, either present by their nature or created with the removal of microdroplets and node defects, can subject the substrate to environmental exposure and facilitate corrosion acceleration. Upgraded defect-free coatings are urgently needed for application in biomedical instruments and for creating barrier layers in micro- and nanoelectronics. It is also necessary to develop new materials and compounds for studying physical effects. Therefore, it is of great importance to understand the nature of the formation of defects in a material and their influence on the coating characteristics.

In Ref. [124], multilayer Ti/TiN coatings were obtained by the magnetron sputtering method. The substrate temperature was 400 °C and the working pressure was 0.53 Pa. The transition from Ti to TiN during deposition was achieved by regulating the nitrogen flux without interrupting the plasma flow (9.3 sc $\mathrm{cm}^3\ \mathrm{min}^{-1}$ of Ar for Ti and 4/5.6 sc $\mathrm{cm}^3\ \mathrm{min}^{-1}$ of Ar/N_2 for TiN), as a result of which a gradient interface was produced. In this way, two series of samples were fabricated, the first with a grounded substrate and the second with a similar modulation period and an applied bias potential of -100 V.

The X-ray diffraction patterns of the samples are presented in Fig. 19a. It was found that in the absence of a negative potential on the substrate during the sputtering, the growth of layers occurs in the directions [111] and [200]. When a negative potential of -100 V is switched on, the nitride layer growth texture is changed, with the predominant (111) orientation, which is more stable. The X-ray diffraction peaks corresponding to titanium layers in all samples demonstrated a mixed (002) and (101) orientation, although it could be noted that upon applying a potential of -100 V the (101) peak was practically absent.

Figure 19b shows the mean size of grains calculated for the directions (101), (002) of titanium layers and (111), (200) of titanium nitride layers. For the TiN layers along the direction (111), the mean grain size is within the range 13–18 nm, independent of the applied potential. In most cases, the grain size decreases with an increase in the bias potential [125, 126]; however, in Ref. [125], it was assumed that for TiN layers the great orientation change in the (111) direction is

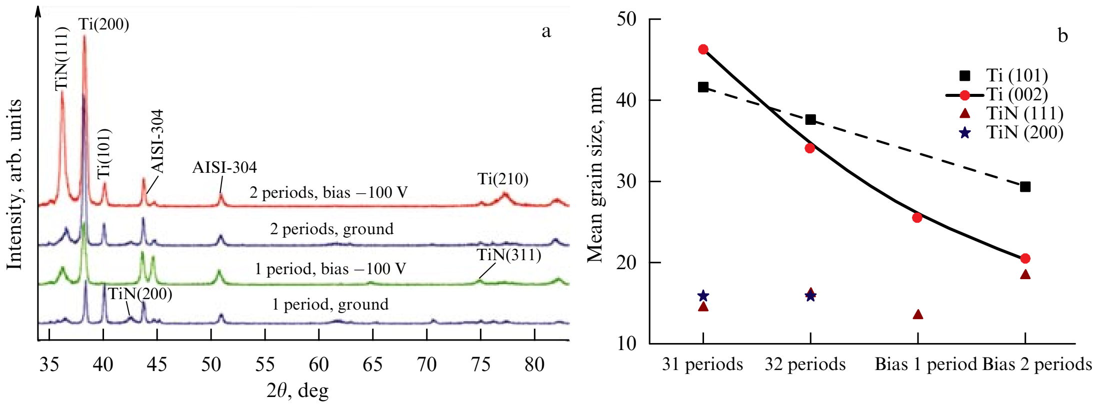

Figure 19. (a) Diffraction patterns of samples with different numbers of Ti/TiN periods with a negative substrate bias potential of −100 V and without bias. (b) The mean grain size calculated from FWHM (*hkl*) of the diffraction peaks [125].

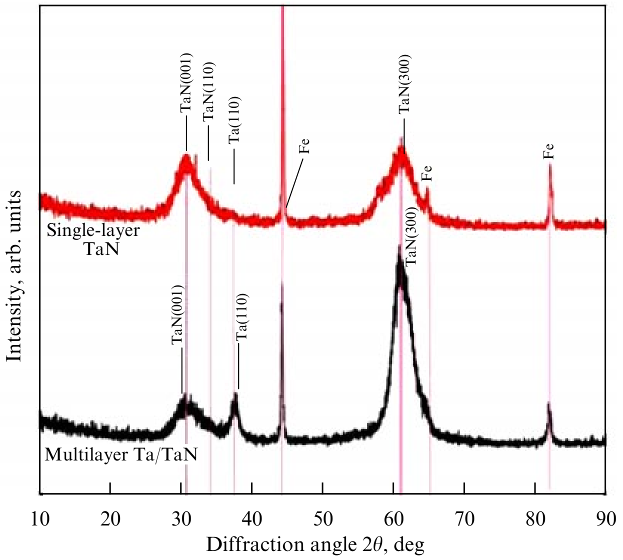

Figure 20. Areas of diffraction spectra of TaN single-layer coating and multilayer Ta/TaN coating [127].

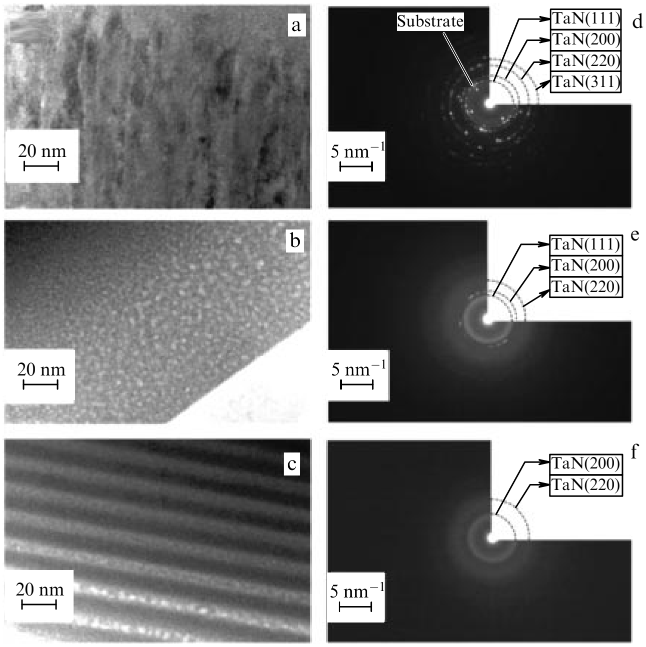

Figure 21. TEM images of the coatings: (a) c-TaN, (b) a-TaN, (c) Ta/TaN. Electron diffraction patterns from selected regions of the coatings: (d) c-TaN, (e) a-TaN, (f) Ta/TaN [128].

reduced by competitive grain growth in other directions, which facilitates the change in grain sizes. In the case of the (002) orientation of Ti films, the calculated grain size decreased in the samples deposited in the presence of the bias potential (Fig. 19b) with various numbers of bilayers. The transition from TiN to Ti was implemented without interrupting the film growth; therefore, every layer substantially inherits structural features of the preceding one. Multilayer coatings of six periods deposited under similar conditions with a grounded substrate had a mean grain size of 27 nm for Ti (002), which is lower than in the coating consisting of four layers (two periods) that amounts to 34 nm.

In Ref. [127], the method of reactive magnetron sputtering was used to obtain multilayer nitride coatings using the example of Ta/TaN systems. A series of nitride coatings was considered with different phase compositions: a-TaN, c-TaN, and a multilayer TaN coating with a mixed phase composition. The working pressure was fixed at a level of 0.6 Pa, the total gas flow being 20 cm^3 min^{-1}. The ratio of Ar and N_2 flows was controlled at 18/2 and 12/8, which allowed the formation of coatings with different compositions and microstructures. A multilayer coating was obtained by sequential deposition of c-TaN ($Ar/N_2 = 18/2$) and a-TaN ($Ar/N_2 = 12/8$) layers forming a bilayer 20 nm thick with a total coating thickness of about 1 μm.

The diffraction patterns of TaN and multilayer Ta/TaN coatings are presented in Fig. 20. A pronounced reflex from the Ta (110) phase at an angle of 37.5° is present in the multilayer coating sample. In the single-layer coating, the (110) peak is substantially smaller because of the TaN (110) planar reflex. The peaks of hexagonal phases TaN (001), TaN (110), and TaN (300) at angles of 32°, 35° and 62°, respectively, were also found. The multilayer Ta/TaN sample possesses a more pronounced TaN (300) peak, which is explained by higher ion energies (20 keV in the DC mode) when using the method of reactive magnetron sputtering with ion implantation.

For a better understanding of the structure and phase composition of the deposited coatings, a TEM analysis of the a-TaN and c-TaN phases and the multilayer Ta/TaN coating was carried out. As is seen from Fig. 21, the c-TaN single-layer coating is a crystalline phase of FCC δ-TaN with

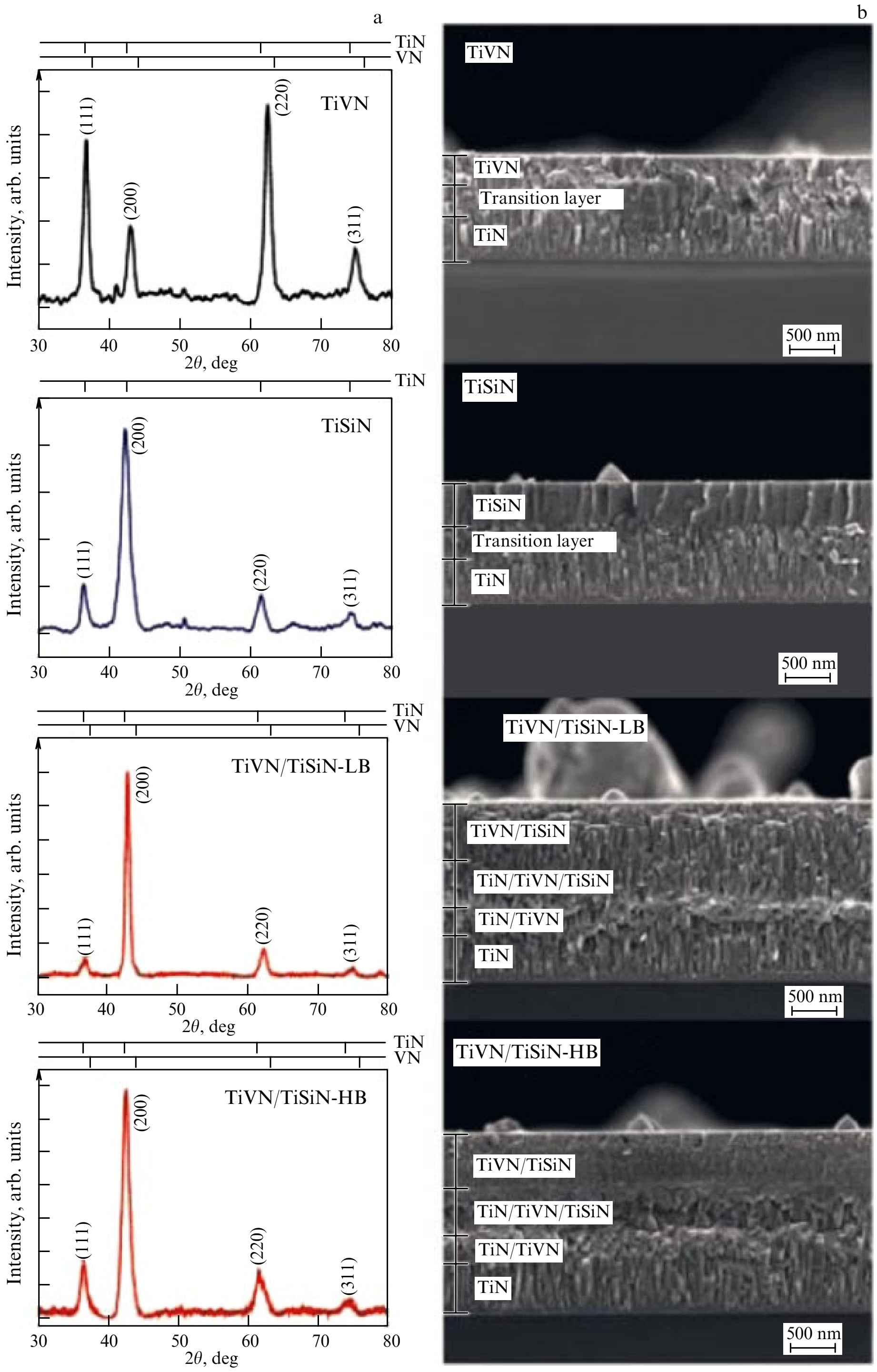

Figure 22. X-ray diffraction spectra (a) and images of cross sections (b) for single-layer TiVN, TiSiN, and multilayer TiVN/TiSiN coatings [129].

predominant orientations (111), (200), (220), and (311). In the microphotograph (Fig. 21a), the columnar structure of c-TaN is clearly seen, in contrast to a-TaN, which has an amorphous microstructure with partial inclusions of crystalline TaN (Fig. 21b). When growing the a-TaN/c-TaN multilayer structure, there is no sufficient space in the a-TaN layers for the wide-range formation of the crystalline TaN phase.

The next stage of the analysis of the quantitative composition effect on the coating properties is to proceed from combinations of single-component and double-component layers to compounds that are more complex. The authors of Ref. [129] proposed doing so from the basic and widely used titanium nitride to a more complex combination of multilayer TiVN/TiSiN coatings. During the magnetron sputtering, the layers of TiN and TiVN were first deposited to improve the adhesion linkage between the coating and the substrate, and then the multilayer TiVN/TiSiN coatings were deposited for 50 min. To accelerate the sputtering by plasma ion flow, a negative potential was applied to the substrate, which appeared to also be an efficient means of controlling the coating properties. Two kinds of TiVN/TiSiN coatings were obtained: with a low bias (LB) potential of −30 V (referred to below as TiVN/TiSiN-LB) and with a higher bias (HB) potential of −180 V (TiVN/TiSiN-HB).

Crystalline structures of single-layer (TiVN, TiSiN) and multilayer (TiVN/TiSiN-LB and TiVN/TiSiN-HB) coatings were investigated using the method of grazing incidence X-ray diffraction (GI-XRD); the results are illustrated in Fig. 22a. All samples demonstrate the formation of a typical cubic B1-NaCl structure. The TiVN diffraction peaks correspond to the planes (111), (200), (220), and (311). The lattice parameter for TiVN amounts to 0.421 nm, which is an intermediate value between the cubic lattice parameters of TiN (0.424 nm) and VN (0.414 nm) [129, 130]. The deposited TiSiN coating demonstrates the B1-NaCl crystalline structure of TiN with the lattice parameter 0.426 nm; no peaks of the Si_3N_4 crystal lattice were found. It is worth noting that the diffraction patterns testify to the formation of nitrides in a single-phase solid solution (only one group of fcc structure peaks manifests itself) [131–134]. The multilayer coatings TiVN/TiSiN-LB and TiVN/TiSiN-HB also possess the B1-NaCl crystal structure. The basic peaks corresponding to the planes (111), (200), and (220) in the NaCl crystal structure are observed. The cubic phase stabilization is caused by the growth of TiVN/TiSiN on cubic TiN and TiVN interlayers. In multilayer films, different growth directions of fcc grains manifest themselves, which implies a coherent structure of alternating TiVN and TiSiN layers. The XRD peaks shift toward smaller angles under an increase in the bias voltage. Similar results were obtained in [135–137]. Mutual competition of atomic deceleration, enhanced mobility of adatoms, and repeated sputtering under an increase in the bias voltage, on the whole, determine the microstructure of resulting coatings. The atomic deceleration gives rise to a redistribution of atoms in the crystal lattice and internal stresses in the coating. The intense ion bombardment causes collision processes between atoms, enhancing their mobility. Such an increase in the mobility of adatoms causes increased growth in the crystallographic directions (100), (111) [138, 139].

Figure 22b shows cross section images of single-layer TiVN, TiSiN and multilayer TiVN/TiSiN-LB and TiVN/TiSiN-HB coatings, in which it is possible to observe a columnar microstructure, typical of coatings deposited at low energy and under the condition $H/E < 0.1$ [11–13, 15]. The images were obtained using field emission scanning electron microscopy (FE-SEM).

Additional EDS analysis showed that TiVN and TiSiN coatings comprise an intermediate layer of TiN and a transition layer with a high content of Ti. Between the transition layer and the upper layer of TiSiN, individual interfaces can be seen. In the TiSiN coating, the addition of Si provoked the growth and repeated nucleation of grains, which ultimately yields a more compact and dense structure [140, 141]. The TiVN/TiSiN-LB and TiVN/TiSiN-HB coatings obtained by combined sputtering of Ti, TiV, and TiSi in nitrogen also possessed an intermediate layer of TiN and transition layers at interfaces. The upper TiVN/TiSiN-HB layer deposited at a high bias potential of −180 V has a denser columnar structure.

3.2 Effect of residual pressure on the coating characteristics

The interrelation between residual stresses, microstructure, elemental composition, and conditions of film deposition has been the subject of intense research for many years. In films obtained using PVD methods, many authors reported on the role of such parameters as substrate temperature, pressure and composition of the working gas, distance between the source and the substrate, substrate bias, and angular distribution of adatoms, which is partially considered in the previous sections. Although there is still no complete fundamental understanding of relevant physical mechanisms, a great amount of knowledge was accumulated and a variety of experimental results were obtained during recent years of intense studies [142–145]. Analyzing the literature data, it is possible to suggest that, at low temperatures of the substrate, the influence of volume diffusion is insignificant, and the main role in the growth dynamics is played by the mobility of adatoms on the surface of deposition [146]. Thus, the normalized momentum imparted to the growing film mainly determines the microstructure and internal stresses of a thin film,

$$P_{\mathrm{n}}^{*} = \gamma (ME)^{1/2}\,, \tag{3}$$

where M is the ion mass, E is the ion energy, γ is the ratio of ion and adatom fluxes, and P_{n}^{*} is a function of several deposition parameters [142].

At low values of P_{n}^{*} (e.g., in the case of sputtering at high gas pressure, when the gas is thermalized), the surface mobility of adatoms is small; therefore, the films are characterized by a porous columnar microstructure and possess maximum roughness of the surface (corresponding to the Thornton structure zone diagram [119]). As a result of interatomic interactions in the gaps between columnar grains, the appearance of tensile stresses should be also expected [147, 148]. At higher values of P_{n}^{*}, the surface mobility of adatoms increases at the expense of the increase in kinetic energy and cascade collisions with particles bombarding the film. At higher adatom mobility, the cavities are destroyed to dimensions comparable to the range of action of interatomic forces and, thus, the tensile stress reaches a maximum. This is accompanied by an abrupt transition from tensile to compressive stress, and a microstructure of a T-type zone consisting of densely packed columns is formed [149]. At such values of P_{n}^{*}, the interatomic forces that would otherwise give rise to tensile stress decrease [150], since the size and number of cavities are additionally reduced due to the high mobility of adatoms. The residual stresses in the film substantially affect its adhesion to the substrate and frequently lead to exfoliation [151]. Therefore, the energy required to form flexible hard films with increased crack resistance must come directly to the growing film and facilitate the conditions for volume diffusion. Such conditions can be achieved by changing the pressure of working gas atoms and ion mobility.

The effect of gas impurities on the stress in deposited films was studied in a number of papers, in particular, a transition of the internal stress state from compression to tension was observed upon the introduction of a reactive gas and change in its concentration; this is explicitly traced in the case of oxide coatings [152–154]. Nevertheless, in all studies, it was found that the stress in a film greatly depends on the partial pressure of impurity gases and correlates with the number of impurity atoms implanted onto the coating. It is worth noting that a rigorous explanation of the effect of partial pressure and impurity atoms on the growth kinetics of a film, particularly a multilayer one, is complicated by multiple factors (lattice distortions due to impurity interstitial atoms, the effect of impurity atoms on the mobility of adatoms) and requires further investigation.

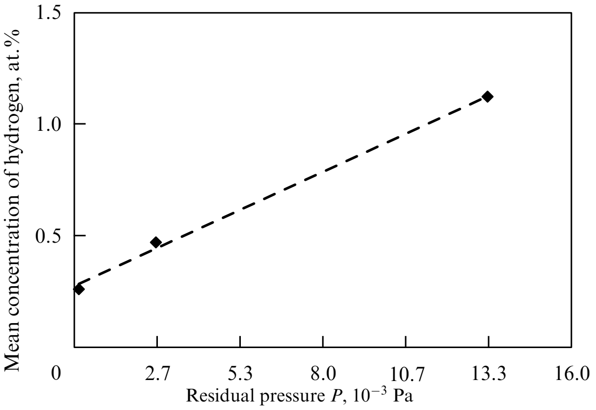

Figure 23. Dependence of the averaged hydrogen concentration in a multilayer Mo/Si coating on the residual pressure in the chamber [142].

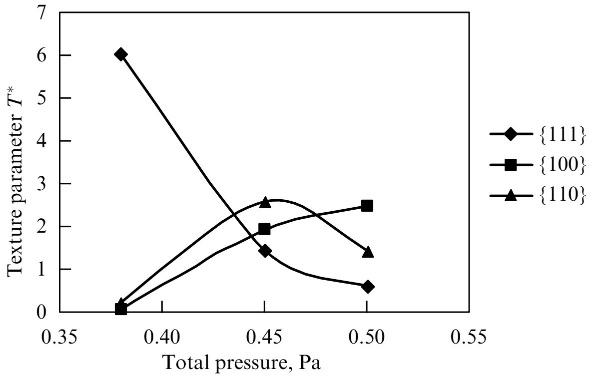

Figure 24. Influence of the total pressure P_T on texture development in TiAlN/CrN coatings deposited at $V_b = -85$ V [76].

As an example, multilayer Mo/Si films obtained using the magnetron sputtering method were considered in [142]. In this study, the stress in the coating (calculated using Stoney's formula based on the surface curvature) was found to be strongly dependent on the residual pressure in the chamber. In particular, it was found that for multilayer films of 40 periods with a layer thickness of ~ 4.3 nm for Si and ~ 2.6 nm for Mo the compressive stress in the film increases from -280 to -450 MPa when the residual pressure in the chamber decreases from 1.3×10^{-3} to 8.0×10^{-6} Pa. It is remarkable that in multilayer films with thicker Mo layers this dependence increases. It was discovered that the concentrations of oxygen and carbon impurity atoms measured by electron Auger spectroscopy amount to less than ~ 0.5 at.% in all samples, whereas the mean hydrogen concentration, determined from the measurements of He beam (2.6 MeV) scattering, varies from ~ 0.3 to ~ 1.2 at.% (Fig. 23), directly proportional to an increase in the chamber pressure and Mo layer thickness.

The general principle of texture development in nanoscale multilayer coatings follows similar tendencies as that in single-layer coatings. In particular, the principle of TiAlN/VN coating formation largely corresponds to the direction of TiN coating growth in the case of magnetron sputtering. In Ref. [76], it was shown that at $V_b = -75$ V the $\{110\}$ texture is developed, whereas in the TiN coating the $\{110\}$ texture is developed at $V_b = -50$ V. As described in Section 3.1, one of the main effects of bias voltage increase is the enhancement of adatoms mobility. Therefore, the direct dependence between the bias potential on the substrate and the texture of the obtained coating is distorted when there is a change in the coating material and deposition parameters, e.g., the pressure P_T in the chamber. Therefore, it can be hypothesized that during deposition the sequence of texture development will be similar, but the bias potential at which particular structures develop changes depending on the coating material and deposition parameters. This is confirmed by the comparative analysis [76], in which TiAlN/VN nanoscale multilayer coatings were deposited at higher total pressure P_T and bias voltage $V_b = -85$ V (Fig. 24). The increase in the total pressure P_T from 0.38 to 0.45 Pa led to a change in the texture from $\{111\}$ to $\{110\}$. A subsequent increase in the total pressure gave rise to an enhancement of the $\{100\}$ texture component, because at the same bias potential an increase in the total pressure reduces the energy of bombarding ions and, therefore, has the same effect on texture formation as a decrease in the bias voltage. Therefore, the observed texture at $V_b = -85$ V and a total pressure of $P_T = 0.45$ Pa is similar to that grown at $V_b = -75$ V and $P_T = 0.38$ Pa, when in both cases the energy conditions lead to the formation of $\{110\}$ texture.

3.3 Effect of an interface width increase and transition layer formation on the properties of multilayer coatings

The authors of Ref. [104] considered the properties of single-layer and multilayer CrAlN/SiN$_x$ coatings with various bilayer thicknesses, as well as the influence of an SiN$_x$ amorphous layer on the film growth texture. From the X-ray diffraction patterns presented in Fig. 25a, it was found that the single-layer CrAlN coating has the B1 fcc structure with a preferable (111) orientation. In earlier described TiN and CrN coatings, the samples demonstrated an identical fcc structure and a similar preferable (111) orientation when the coating thickness exceeded 200 and 180 nm, respectively [155, 156]. The preferable orientation was interpreted as a result of minimization of the total energy, including the surface and point energy, during deposition [157]. As shown in Fig. 25a, at an SiN$_x$ layer thickness of 0.3 nm, they periodically penetrate into the CrAlN layers, preserving the

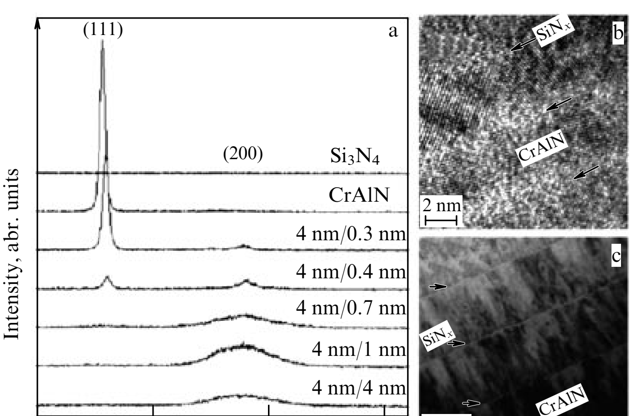

Figure 25. (a) Diffraction patterns of single-layer and multilayer CrAlN/SiN$_x$ coatings at different values of the SiN$_x$ layer thickness; (b) TEM images of multilayer coatings with $l_{\mathrm{CrAlN}}/l_{\mathrm{SiN}_x} = 4$ nm/1 nm; (c) $l_{\mathrm{CrAlN}}/l_{\mathrm{SiN}_x} = 100$ nm/1 nm [104].

(111) orientation. This means that the epitaxial growth of SiN_x has practically no effect on the growth of CrAlN grains. The deformational crystallization of SiN_x was found only on a superfine scale ($l_{SiN_x} \leqslant 0.3$ nm in [6]). From the data in Fig. 25a, it is also possible to note that broadened diffraction peaks and the preferable orientation changing from (111) to (200) are characteristic of coatings with a layer of SiN_x more than 0.7 nm thick.

Nitrides of transition metals, such as TiN and CrN, as a rule, grow along the densest plane (200) to reduce the surface energy. The broadened (200) peaks indicate interrupted growth of the CrAlN layer, the interruption occurring with each next SiN_x layer. A grain size of less than 4 nm was found in coatings with SiN_x layers more than 0.7 nm thick. In Ref. [104], it was supposed that the growth of CrAlN grains is limited by two adjacent disordered layers of SiN_x. Figures 25b, c present TEM images of $CrAlN/SiN_x$ cross sections ($l_{SiN_x} = 1$ nm). From high-resolution images of grains in the layers of CrAlN, the growth limitation by the amorphous SiN_x interlayer is obvious.

From the results in [104] for three different $CrAlN/SiN_x$ microstructures with thin layers of SiN_x ($l_{SiN_x} \leqslant 0.3$ nm), it follows that columnar growth is continuous, whereas a thicker layer of SiN_x can interrupt such growth directivity. Since CrAlN is recrystallized and grown on a disordered layer of SiN_x, the size of a CrAlN grain can be controlled by thickening the CrAlN layer.

This affected the physical-mechanical characteristics of coatings. The hardness of a single-layer CrAlN coating amounted to 27.1 GPa, and a multilayer coating with fine grains (about 21.8 nm) demonstrated an improved value of hardness, equal to 31.6 GPa. With a further decrease in grain size, the hardness considerably decreased, and the minimal hardness of 21.6 GPa was even lower than that calculated using the mixing rule. In coatings with a grain size of less than 21.8 nm, the motion of dislocations is easier because of an increased degree of structure disorder (according to the inverse Hall–Petch relation), including the SiN_x layer itself and the boundary of grains in the CrAlN layers [158]. Therefore, the corresponding grain size in the $CrAlN/SiN_x$ coating in this study amounted to 21.8 nm, and the expected bilayer thickness would be $l_{CrAlN}/l_{SiN_x} = 100$ nm/1 nm.

The authors of Ref. [159] obtained TiAlN/CrN coatings with thicknesses of alternating layers of 8 and 17 nm using the vacuum arc method. According to X-ray diffraction analysis, the TiAlN/CrN coating has a B1-NaCl crystal structure with the preferable orientation (111). The main structure peaks testify to the equilibrium position of TiAlN and CrN phases. The asymmetry of the texture peak (200) is due to overlapping of reflection amplitudes from the TiAlN and CrN phases. It was found that CrN has a higher reflection intensity in the (200) plane of a multilayer TiAlN/CrN coating with a thickness of 8 nm of alternating layers. This is evidence of the fact that CrN layers affect the {200} texture development in TiAlN/CrN systems with different thicknesses of layers. The change in the width of the layers also causes competitive growth of CrN and TiAlN phases in a multilayer TiAlN/CrN coating.

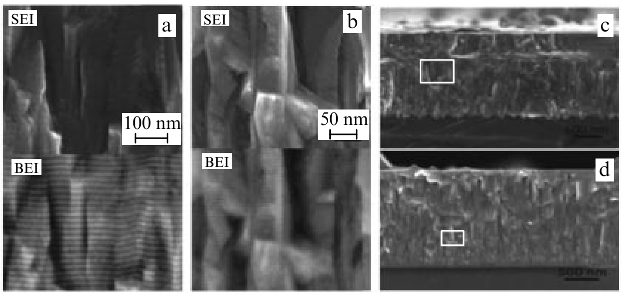

Figure 26. TEM images of the cross section of TiAlN/CrN multilayer coatings with thicknesses of alternating layers $\lambda = 8$ nm (a, b) and 17 nm (c, d) [159].

Figure 26 shows cross section microphotographs of deposited TiAlN/CrN coatings ($\lambda = 8$ and 17 nm). The coatings have a dense columnar structure; however, because of ion-induced processes, aggregates of point defects and small dislocation loops arise, which leads to repeated continuous nucleation of new grains in the process of growth and disturbance of the columnar structure of the coating. Microphotographs of the TiAlN/CrN cross section emphasize the difference between the layers of TiAlN and CrN: the CrN layers have a brighter contrast, since they reflect a greater number of electrons. For TiAlN/CrN system types with both $\lambda = 8$ and 17 nm, a layer of CrN was deposited between the substrate and the coating as a transition layer. The most distinct layered structure is observed in the TiAlN/CrN coating with the greater bilayer thickness (17 nm); in the case of $\lambda = 8$ nm, the layer boundaries have blurred view due to the appearance of interlayer diffusion.

The multilayer architecture of functional coatings allows the size of crystallites to be affected, which leads to a change in their mechanical characteristics. The size of crystallites and lattice deformation for TiAlN/CrN were calculated in accordance with the Williamson–Hall plot. In comparison with single-layer TiAlN and CrN coatings, the crystallite size in a multilayer TiAlN/CrN coating decreased by 11 nm and amounted to 31 nm (for $\lambda = 17$ nm) and 38 nm (for $\lambda = 8$ nm). The decrease in the grain size is due to the formation of interfaces between the layers [160]. A multilayer coating with a smaller layer thickness should have a proportionally smaller grain size. The increase in the crystallite size in TiAlN/CrN ($\lambda = 8$ nm) is most likely due to the diffusion of atoms between layers during deposition. Depending on the energy conditions of deposition, coatings can be in amorphous and nanocrystalline states, as well as in a nanocrystalline state, preferably with an oriented (columnar) structure. For nitride coatings based on the extended group of refractory metals, the tendency to form two preferable growth directions with the plane (111) or (200) is relevant.

On the other hand, interfaces in a multilayer structure block the movement of dislocations by inducing the initiation and propagation of cracks. The application of alternating nanocrystal and amorphous layers removes this drawback and allows achieving a high coating strength [12] (see, e.g., the nc-*Me*N/a-Si_3N_4 system (*Me* — metal) [103]). In this architecture, instead of blocking deformations, the amorphous layer acts like a 'glue', making it possible to avoid the inverse Hall–Petch law. In his review [161], Zhang specified the main mechanisms of nanocomposite multilayer coatings in a way similar to the existing trends in ceramic (bulk) samples [162], such as strengthening due to the creation of a plastic phase weakening the strain field near an incipient crack, as well as overcoming crack formation by using plastic phase links. The techniques of strengthening by phase transition under a load, strengthening by compression stresses at the expense of the contribution from carbon nanotubes, as well as the creation of a gradient layer, are of no less importance.

4. Application of multilayer coatings

4.1 Wear and friction

Perfect tribological properties of materials are mainly defined by high hardness, improved fracture toughness, and surface homogeneity. In this aspect, single-layer/single-phase microstructured coatings demonstrate improved tribological characteristics compared to bulk materials. However, these coatings are not suitable for cutting tools [163, 164]. The coatings are destroyed due to excessive mechanical and chemical damage because of low wear resistance and high friction. Therefore, the tribological characteristics can be improved only by increasing the strength and fracture toughness [165, 166].

Films of TiN, CrN, and TiAlN are more and more frequently used under rigid industrial conditions thanks to their attractive characteristics, including high resistance to oxidation, corrosion resistance, and a low friction coefficient [167]. However, their application under high-temperature conditions still meets with substantial technical difficulties.

Super-hard multilayer coatings have been considered as promising materials for tribological applications for a long time. The mechanical properties of such coatings are improved due to unique combinations of phases and the interphase architecture.

In review [168], it is shown that, as a result of combining materials with the appropriate design strategy, multilayer coatings can be adapted to reduce the friction coefficient and to enhance wear resistance for application in various tribological systems. Taking into account the wide spectrum of materials and methods used to fabricate multilayer coatings for tribological applications, it is necessary to deposit one or a few intermediate layers on the substrate before depositing the main coating, which considerably enhances the adhesion between the coating and the substrate and improves the tribological characteristics [169].

In Reference [170], multilayer nitride coatings based on transition metals TiN/CrN, TiN/ZrN, and TiN/WN were deposited on the most technologically widespread substrates of Si(100) and stainless steel (316LN) using the reactive magnetron sputtering method. As a result of tribological tests, the wear rate of a TiN/ZrN multilayer coating deposited on steel appeared to be lower than in a similar sample on a silicon substrate (Fig. 27). Similar results were obtained when comparing wear rates of TiN/WN coatings. The authors concluded that all the obtained coatings possess enough internal energy to resist shear strain in the course of sliding. In this case, the internal stress at the coating-substrate interface prevails over the contact stress that exists between the slippage boundaries [170].

Optical and TEM images of coating wear morphologies are presented in Fig. 28. Samples with a TiN/CrN coating demonstrated a fast removal of the first layer (CrN), which can occur because of high contact pressure during the initial cycles of sliding, when the contact area is smaller. The contact area increases with the number of cycles, which, in turn, leads to strain hardening; therefore, the resistance to plastic deformation increases [170].

The transfer of the oxide layer of the metal of the TiN/CrN and TiN/ZrN coatings is confirmed by TEM images of wear tracks (see Fig. 28). The broad wear track of the TiN/ZrN sample (Fig. 28b, e) is explained by the fact that the ball material wear is transferred to the coating. Ultimately, the TiN/WN multilayer coating appeared to possess the highest wear resistance among all samples. No significant wear was observed on the friction surface of the track, which is due to high fracture toughness of the multilayer TiN/WN coating (Fig. 28c, f); however, the contact area was increased (almost two times greater than in other samples) because of the high wear of the steel ball. High wear resistance and a low friction coefficient in the multilayer TiN/WN coating are directly related to superhardness, equal to 50.4 GPa. Such perfect tribomechanical characteristics are due to strain hardening, appearing due to the lattice difference at the TiN/WN interface [170].

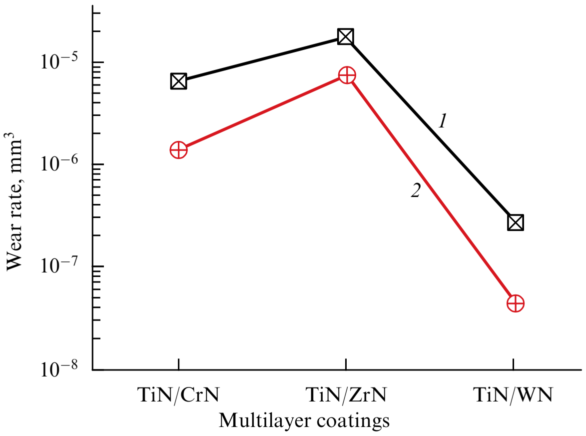

Figure 27. Wear rate of TiN/CrN, TiN/ZrN, and TiN/WN multilayer coatings deposited on an Si substrate (*1*), and on a steel substrate (*2*) [170].

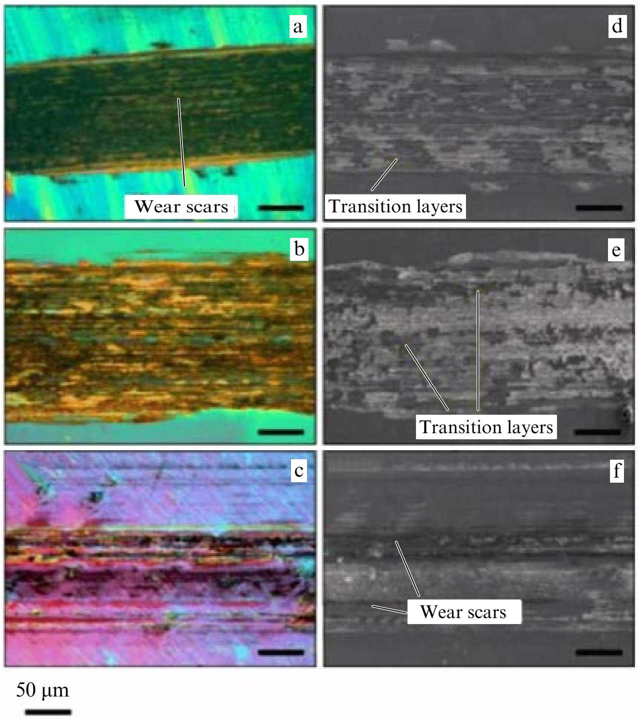

Figure 28. Optical and TEM images of wear tracks on multilayer coatings (a, d) TiN/CrN, (b, e) TiN/ZrN, and (c, f) TiN/WN deposited on 316LN steel substrates [170].

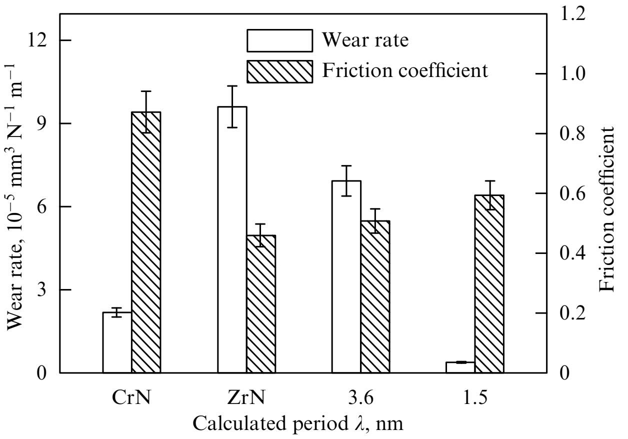

Figure 29. Dependence of the friction coefficient and wear rate on the modulation period of ZrN/CrN multilayer coatings obtained at $P_N = 2.6 \times 10^{-1}$ Pa, $T_s = 200\,^{\circ}$C, $V_b = 200$ V [111].

In Ref. [112], the wear resistances of multilayer ZrN/CrN coatings obtained by DC magnetron sputtering on silicon substrates were compared, depending on the modulation period. An Si_3N_4 ceramic ball was used as a counterbody. The wear measurement was performed following the 'ball–disc' scheme under a load of 2 N; the sliding velocity was 1000 revolutions per minute. Figure 29 presents the friction and wear coefficients for samples with different modulation periods. The obtained experimental data testify to the fact that the wear coefficient of the multilayer coating with the modulation period of 1.5 nm attains the value of 0.3865×10^{-5} mm^3 N^{-1} m^{-1}, which is 6 to 24 times higher than for ZrN and CrN coatings.

Using a scratch test, the adhesion strength of ZrN/CrN coatings obtained in [171] was analyzed. The study is based on scratching the coating surface by continuously pressing the indenter. The depth of indenter pressing was 10–15% of the total coating thickness (800 nm–1μm). Figure 30 presents scratch scans before and after the test and images of the coating surface after the test. A comparison with mononitride ZrN and CrN coatings is executed. The first appearance of cracks related to cohesive failure of coating was fixed at loads > 50 mN. However, the appearance of cracks was sporadic. No signs of adhesive fracture were observed till the load reached 85 mN. The critical load of adhesive fracture amounted to 100 mN.

The effect of the period of bilayer modulation λ on the tribological characteristics of a multilayer CrN/ZrN coating was studied in Ref. [85]. Two samples of a CrN/ZrN multilayer coating ($\lambda = 66.7$ and 11.7 nm) were prepared for tribological testing. Similar to other multilayer systems, the process of measuring the friction coefficient can be divided into two stages, the initial mode and the steady-state one. The sharp increase in the friction coefficient at the initial stage can be due to the action of oxide layers formed on the coating surface and the change in contact stresses. The friction coefficient and the volume of worn material become smaller with a decrease in the modulation period λ. For the CrN/ZrN multilayer system with $\lambda = 66.7$ nm, the friction coefficient was 0.32 and the wear coefficient was 5.4×10^{-6} mm^3 m^{-1}, whereas for $\lambda = 11.7$ nm the friction and wear coefficient decreased to values of 0.3 and 5.5×10^{-7} mm^3 m^{-1}, respectively.

To analyze the coating morphology in more detail, a 3D model of the sample surface after the tribological testing was constructed (Fig. 31). In this model, a dip (groove formation) in the middle of the wear track and the transfer of material to the track periphery are clearly seen. Using EDS analysis, it was determined that W from the counterbody surface is present in the material.

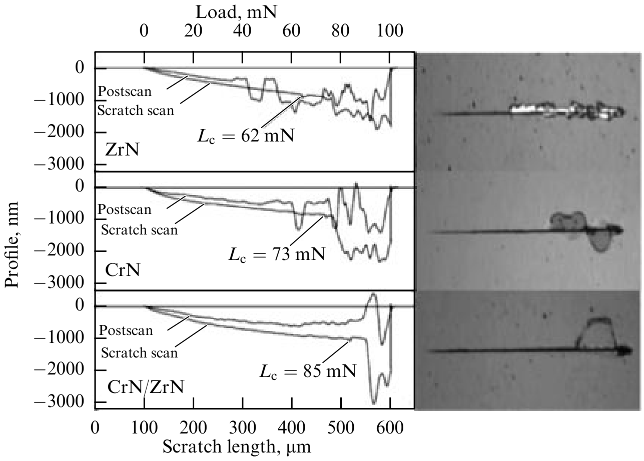

Figure 30. Scratch-scanning profiles and photographs of surfaces of ZrN/CrN multilayer coatings after experiment [171].

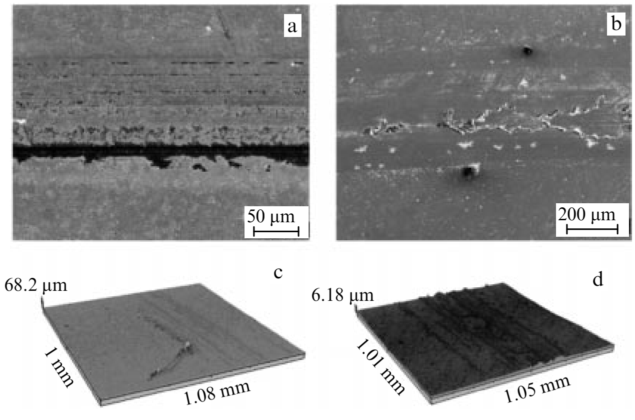

Figure 31. Surface microphotograph and 3D image of CrN/ZrN multilayer coating after a tribological test: (a, c) $\lambda = 66.7$ nm; (b, d) $\lambda = 11.7$ nm [110].

The high temperature arising in the process of dry friction led to the pressing of counterbody particles into the coating surface and the formation of oxides, which affected the values of friction coefficients. In Fig. 31, it is possible to see a broader wear track and uniform cohesion character of material abrasion. The authors of [110] ascertain that strong abrasion testifies to effective barrier properties of the given coating, preventing the destruction of a cutting tool caused by plastic deformations from the formation of microcracks.

To determine the wear mechanisms of a multilayer TiN/TaN system, the authors of [172] analyzed the morphology of coating samples with different periods of modulation. It is worth noting that the wear track mainly consists of grooves, and the track width decreases with increasing hardness of a multilayer coating. Transfer of a minor material amount from the grooves on the wear track is observed during tribological testing and the appropriate EDS analysis. The occurrence of cleavages and material transfer on the surface of wear tracks can be due to high compression stresses inside the coating. Increasing the modulation period removes these phenomena. Thus, although the friction coefficient in a single-layer TiN coating is lower than in a multilayer TiN/TaN one, the wear resistance of the latter is significantly higher.

4.2 Deformation

Investigations of the mechanical performance of multilayer coatings and their implementation were preceded by intense studies of the role of various parameters in the mechanical properties of nanostructured metals and alloys [173–176]. According to the data presented, it is possible to enumerate the key factors affecting plastic deformations in a nanoscale multilayer structure: the thickness of individual layers, the relationships among multilayer component thicknesses, the type and structure of interfaces, and the differences among the mechanical properties of individual layers. The effect of the interface on the mechanical properties dominates, particularly when the thickness of an individual bilayer is of the order of a few nanometers [35, 53, 177–179]. Interphase boundaries act as a source and/or accumulation site of film defects, such as dislocations and vacancies. Because of the difficulty of vacancy transfer though interfaces, the mechanisms of plastic deformation depend on the type of interphase boundary. Three types of interphase boundaries can be distinguished: coherent, semi-coherent, and incoherent [9, 180]. In the case of coherent boundaries, two adjacent layers of different materials have a similar crystallographic structure and crystal orientation. Two crystals perfectly coincide with high coherent stresses, and the lattice plane is continuous at the interface with a minor mismatch of lattices. In this case, dislocations are transferred to other layers after exceeding the coherent stress barrier.

Semi-coherent interphase boundaries are defined as those between layers with a similar lattice structure, but a greater difference between lattice parameters, exceeding 5%, or with different lattice structures but a small degree of mismatch. The incompatibility of lattices gives rise to the overlapping of some domains with high coherence stress and potential energy. Interphase boundaries with a changed geometry of mismatch dislocations for relaxation of inter-interface stresses facilitate their shift towards the energy-preferable binding site [181]. Because of the great difference between the structures of lattices, under a load, the interphase boundaries act like obstacles to possible sliding, since there is no continuity between two adjacent layers, which often leads to a slight shift of boundaries.

To analyze the deformation and wear resistance, the TiN/TiAlN system [182] was chosen as one of the samples in which the multiplicity of layers does not affect the hardness but improves the operation efficiency under extreme conditions. Low wear rates and a higher resistance to fracture under plastic deformation than in single-layer analogs characterize this system. From the point of view of the deformation process, multilayer coatings have an additional advantage: acting as strain markers that allow visual identification of microscopic deformation mechanisms. Possible deformation modes for a TiN layer include columnar slip, edge cracking, bending, and diagonal cracks [182]. Columnar slip represents the shear of the weakest link in the microstructure, the column boundaries, which are related to vacancies or the free volume. Similarly, bend cracks that propagate towards the surface arise because of tensile stresses due to a mismatch of deformations at the film-substrate interface and terminate at the entry to the compression zone under indentation [183–186]. Thick coatings and soft substrates facilitate the appearance of so-called diagonal shear cracks as a result of columnar shears that not always spread over the entire interface. Being oriented at a small angle to the surface, these cracks exert the most negative influence, since they merge with other cracks and facilitate coating exfoliation [177].

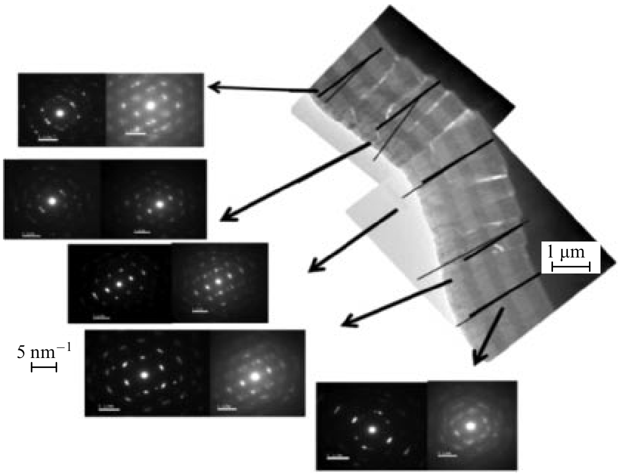

Figure 32. Bright-field image of the diffraction pattern at different parts of the film (in thickness) and an image of the coating cross section [182].

Although most defects of multilayer coatings have already been described, worth special attention are sources of deformations, including the nature of gaps leading to coating cracking. The porosity of films arising due to a small bias potential on the substrate, leading to loose packing of material at the grain boundaries, is considered one of the causes of cracking [123, 187]. It is possible to distinguish the process of deformation initiation for a thin coating, which changes over to a diagonal cracking together with a small amount of columnar shear (deformations) in thicker coatings. This change is explained manly by the columnar boundaries in thin films that are replaced by more equiaxial grains in the case of thick coatings. Also worth attention is the role of material plasticity in reducing cracking in a multilayer film [123].

Multilayer TiN/TiAlN films 10 μm thick with equal thicknesses of TiN and TiAlN were deposited on a substrate of 304 stainless steel using the method of vacuum-arc deposition. Figure 32 (right-hand part) shows a TEM image of the film, in which it is possible to observe the difference between the sliding of columnar texture in the TiN/TiAlN multilayer coating. The multilayer architecture allows tracing the gradual transition from a bend at the surface to one of discrete columnar shear towards the middle of the film, beyond which the layers are rigidly displaced but remain parallel with respect to the initial nondeformed orientation. Electron-diffraction studies show that the coating has columnar grains with the growth direction $\{111\}$ parallel to the interface. Thus, the vector of diffraction $\{111\}$, perpendicular to the interface of grains, can be used to trace the orientation of grains. An insignificant change in orientation in the $\{111\}$ direction is observed, whereas a much greater change in orientation exists near the surface, where grains with the $\{111\}$ texture tend to tilt towards the indentation axis.

To investigate the mechanism of interface sliding and its directions, measurements were carried out on both sides of

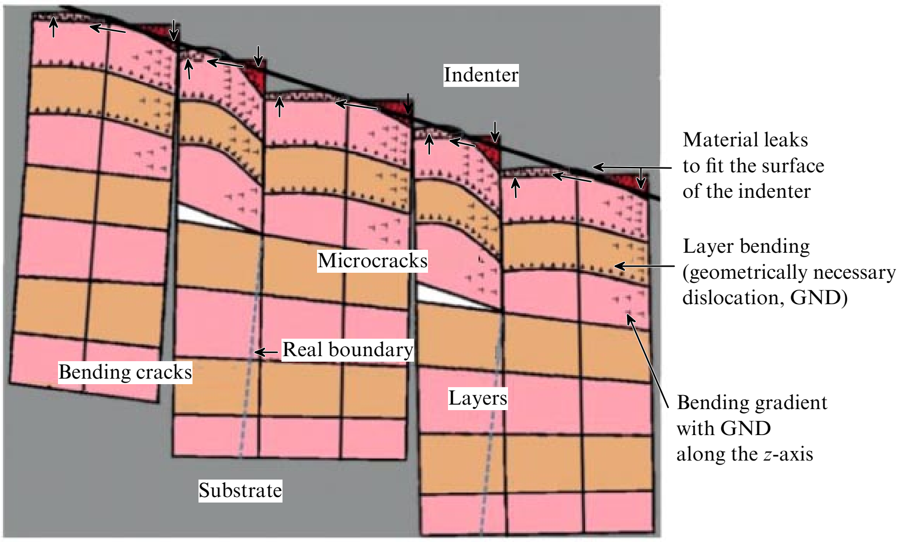

Figure 33. Schematic illustration of stress generation at misfit dislocations along the interface; the mechanism of reducing the stress concentration in the voids of cracks [182].

the boundaries of the columns that represent the sliding, as well as of those that remain unchanged. There are two types of distinguishable boundaries: the first is a binary orientation (rotation through 60° with respect to growing {111}) due to random differences in the packing sequences in the plane during the growth. Thus, one column can grow as AcBaCbAcBaC and the adjacent column as AbCaBcAbC. These twins are different from common ones that manifest themselves in fcc metals, where the boundary between the adjacent twins should be {111}. Here, the interface plane is distorted (see Fig. 32) and possibly contains explicit vacancies, or the N and Ti ratio is nonstoichiometric. Other disorientations will most likely be higher-energy boundaries.

The authors of [172] also consider possible mechanisms of film destruction and analyze the role of multilayer systems in cracking retardation. Indisputable evidence is that the multilayerness does not lead to plasticity in the case of dislocation activity along the layers. In most cases, the compression of layers is observed under hollows, when the deposition conditions (temperature and bias potential of the substrate) are not optimal, due to which cavities arise between the columns that can overlap because of high compression stresses. However, the changes in grain orientation are present even in modified coatings with an improved structure, and they can be due to multiplication of geometrically necessary dislocations (GNDs) at the layer boundaries. Apparently, due to the epitaxial mismatch of lattice parameters between TiN and TiAlN at the interphase surface {111} that can slide, a high density of dislocations is accumulated. The schematic diagram shown in Fig. 33 illustrates how interphase dislocations can slide, decreasing the concentration of stresses at bent columns; in this case, energetically weak interfaces are the first to slide. This means that the sliding of a column, which stopped because of these inflections, can now continue, cracking is inhibited, and the sliding density increases.

The proposed model takes into account the influence of indenter geometry, which facilitates the material flow and accumulation of dislocations. The role of interphase boundaries in stress removal has been analyzed. Alternating layers of TiN and TiAlN near the interfaces have cavities at the boundaries of the columns because of bending stresses. On the surface, the indenter compresses the edges of the columns, and they deform under the action of material flow. The bending of the layers is implemented at the expense of geometrically necessary dislocations, the interphase boundaries acting as sources of these dislocations. In this case, microcracks are formed because of the incompatibility of bending and sliding. References [11–13, 15] show that, to obtain densely packed multilayer coatings without a columnar structure, it is necessary to increase the energy of ions in the process of growth in order to achieve preferable conditions characterized by the relation $H/E \geqslant 0.1$.

4.3 High-temperature oxidation

The growing demand for industrial application of protective multilayer coatings that can function under high temperature loads has led to an urgent need for new studies in this field. For tribological application under high-temperature impact, a multilayer adaptive CrAlN/ZrN coating was considered [73]. Figure 34 presents the results of hardness measurements in a CrAlN/ZrN coating with bilayer thicknesses of 5 nm and 9 nm. The hardness of the coating with $\lambda = 5$ nm is

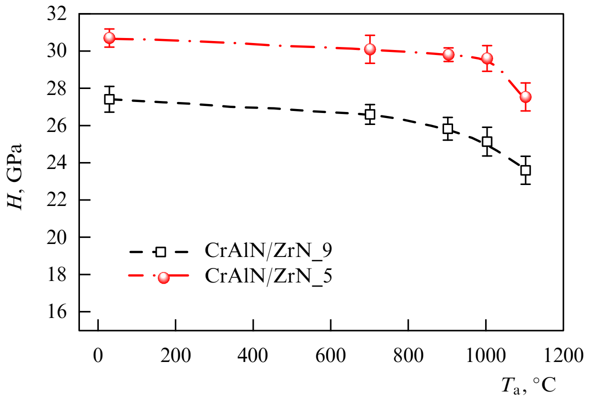

Figure 34. Results of measuring the hardness of a CrAlN/ZrN coating ($\lambda = 5$ and 9 nm) after thermal annealing in a vacuum [73].

significantly higher than that of the control sample with $\lambda = 9$ nm (30.7 GPa versus 27.4 GPa), which is due to proceeding from nonepitaxial to locally epitaxial growth of layers when the modulation increases to 5 nm [73]. The improvement in mechanical and tribological characteristics of multilayer coatings in the case of epitaxial growth of layers is due to a composition of different strengthening mechanisms (inverse Hall–Petch effect, Koehler model, formation of internal stresses, dislocation movement effect, etc.) [188–191]. The elasticity moduli of CrAlN/ZrN coatings with $\lambda = 5$ and 9 nm amount to 400.3 and 395.9 GPa, respectively. Therefore, at $\lambda = 5$ nm, the coating has a higher value of H^3/E^2 (~ 0.18 GPa) than at $\lambda = 9$ nm (~ 0.13 GPa), which is evidenced by its higher wear resistance [192].

The annealing of CrAlN/ZrN multilayer coatings ($\lambda = 5$ and 9 nm) in a vacuum to 700 °C caused a decrease in hardness due to the processes of recovery and relaxation. With a further increase in the annealing temperature to 1100 °C, the formation of a w-AlN phase and a decrease in nitrogen content in CrAlN layers were revealed, which, in turn, led to a continuous decrease in hardness. Thus, the effect of high temperatures (to 1000 °C) on the CrAlN/ZrN coating ($\lambda = 5$ nm) does not lead to a substantial change in hardness. The local epitaxial growth of layers in a multilayer system impedes the formation of cleavages and cracks, thus increasing the coating-substrate adhesion strength. The adhesion strength of CrAlN/ZrN amounts to 74 N and 86 N for $\lambda = 9$ and 5 nm, respectively.

An extensive and promising topic is the creation of hard and at the same time crack-resistant multilayer structures for operating under extreme high-temperature conditions [117]. This is achieved by alternating hard (nanocrystalline) and soft (amorphous) metallic phases when determining the relation between the bilayer period and the direction of grain growth texture. Amorphous structures have grains with widely spread volumes, which practically allows avoiding contact of the substrate with the external atmosphere, whereas hard layers ensure perfect mechanical parameters and wear resistance. In studies related to the formation of characterization of these systems, it was shown that nc-MeN$_x$/a-Si$_3$N$_4$ structures, where $Me =$ Zr, Ta, Mo, W, and Si–B–C–N, provide temperature stability and protection from oxidation in the ranges from 1000 to 1800 °C [12, 14, 193]. However, to achieve stability of temperature and physical-mechanical properties, much attention is focused on the problem of controlling the stoichiometry during sputtering and elemental redistribution in the high-temperature zone in the process of exploitation. Plasma flows in the process of ion sputtering and deposition determine the internal, temperature, and residual stresses in the coating and at the substrate-coating interfaces; therefore, by controlling the ion energy, it is possible to create functional flexible coatings with $H/E > 1$ on substrates of stainless steel and silicon.

Multilayer nanoscale coatings based on nitrides of transition metals have good physical-mechanical and tribological properties at the expense of forming at least two phases and a large number of interphase boundaries, which hamper the movement of dislocations and reduce the tendency to fracture in the coating material [194, 195]. On the other hand, worthy of attention are nanocomposite coatings with nanocrystalline grains of one phase, while another phase envelops these grains in an amorphous interlayer (α), which increases the resistance to high-temperature oxidation. Moreover, the amorphous interlayer complicates the motion of dislocations, which makes the coating more plastic and reduces the tendency to destruction. In Ref. [196], two kinds of layers, AlN and BCN, are used, which also tend to amorphization at low deposition temperatures, making them promising means for protecting the material from external impacts. Multilayer AlN/BCN coatings were obtained by alternating magnetron sputtering of targets with Al and B$_4$C in an argon-nitrogen atmosphere on a polished Si (100) substrate. The obtained coatings were annealed in a vacuum at temperatures $T_{\mathrm{a}} = 600$, 900, and 1000 °C for 1 hour.

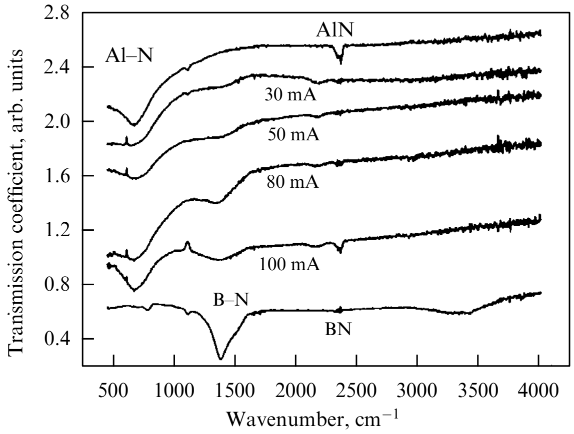

Figure 35. FTIR spectra of single-layer AlN and BCN coatings and a multilayer AlN/BCN coating [196]. The figures an the curves denote the current at the B$_4$C target.

The results of X-ray diffraction studies have shown that deposited single-layer and multilayer coatings are amorphous. In Fourier transform infrared (FTIR) spectra of the obtained coatings (Fig. 35), it is clearly seen [196] that, with an increase in the substrate current $I_{\mathrm{B_4C}}$, the intensity of the absorption band B–N increases and the intensity of the band Al–N decreases. The absence of Al–B and Al–C valence vibration bands testifies to the absence of aluminum compounds with boron and carbon (AlB$_2$, AlB$_{12}$, Al$_4$C$_3$, etc.). In the first approximation, this can be considered to be the formation of distinct boundaries between the amorphous layers α-AlN and α-BCN. It was assumed that a small amount of carbon is present in the form of C-N$_n$B$_m$ compounds. The deposited amorphous AlN/BN coatings demonstrated increased nanohardness (to $H = 16$ GPa), Young modulus (to $E = 260$ GPa), and Knoop hardness (to $H = 27$ Gpa) in comparison with single-layer AlN and BCN coatings, which is explained by the modulation of stresses, associated with the amorphous layers of AlN and BCN.

With an increase in the substrate current $I_{\mathrm{B_4C}}$, the hardness of multilayer coatings increases, reaching the maximum value of 27 GPa for the coating deposited at $I_{\mathrm{B_4C}} = 100$ mA. An increase in $I_{\mathrm{B_4C}}$ increases the interlayer of α-BCN, which, in turn, enhances the stress modulation in the coating, since the stresses differ in the amorphous layers α-AlN and α-BCN. The layer $\alpha =$ AlN is under compression stress, and the layer α-BCN is under tensile stress. The hardness of single-layer α-AlN and α-BCN coatings amounts to 12.2 and 12.8 GPa, respectively. It can be concluded that, in spite of the amorphous structure of multilayer coatings, they are characterized by stress alternation, responsible for an increase in hardness.

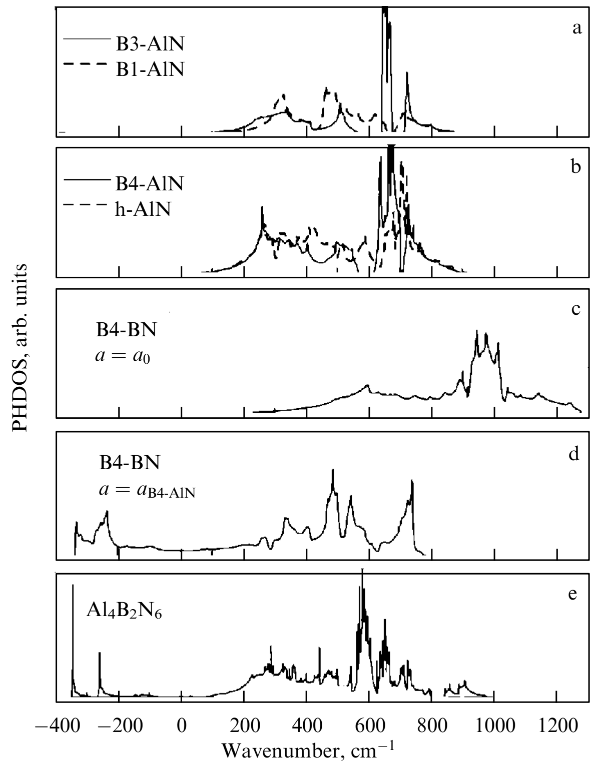

Figure 36. Phonon density of states (PHDOS) for B1-, B3-, B4- (a) and h-AlN (b); B4-BN lattice parameters at equilibrium ($a = a_0$) (c) and for $a = a_{\text{B4-AlN}}$ (d), as well as B4-AlN(001)/BN heterostructure ($Al_4B_2N_6$) (e) [196].

In Ref. [196], the behavior of coatings after annealing was also considered. A considerable reduction in hardness was observed at temperatures beyond 600 °C. Therefore, AlN/BN coatings can be considered thermally stable to 600 °C. Upon a further increase in annealing temperature, a mixing of layers apparently occurs, leading to a decrease in stresses and hardness. Another explanation may be that, at higher annealing temperatures T_a, an increase in the volume proportion of aluminum and boron oxides leads to a decrease in hardness. Based on the results of Refs [197–201], it is possible to ascertain that the oxidation of amorphous nanoscale multilayer coatings is hampered by a low rate of oxygen diffusion in an amorphous matrix, compared to a nanocrystalline one. Thus, amorphous coatings are more efficient in opposing oxidation than are nanocrystalline ones, which is also shown in Ref. [14].

The results of photon partial density of states (PHDOS) calculations are shown in Fig. 36. All calculated AlN and BN structures are dynamically stable in the equilibrium state. However, an increase in the lattice parameters $a_{\text{B4-AlN}}$ leads to the appearance of imaginary frequencies, which testifies to the fact that the epitaxial layers B4-BN cannot form between the layers of B4-AlN, as confirmed by the results of PHDOS calculations for the B4-AlN(001)/BN heterostructure. The phonon spectrum of the heterostructure is seen to possess imaginary frequencies; therefore, the structure is dynamically unstable.

Theoretical studies have shown that in multilayer B4-AlN/BN coatings the B4-BN layer is dynamically unstable; therefore, the layer is amorphous rather than epitaxial, or has another structure different from B4-BN. The coatings in this case are thermally stable to 600 °C at the expense of slowed diffusion in the amorphous interlayer. Thus, amorphous nanoscale coatings are more resistant to oxidation than nanocrystalline ones are.

4.4 Corrosion resistance

A quantitative estimation of corrosion resistance is a difficult task, since the operation lifetime is determined by both the properties of the coating itself and the corrosiveness of environment. In Ref. [85], electrochemical impedance spectroscopy was used to study electrochemical properties of multilayer ZrN/CrN coatings obtained at $P_N = 0.66$ Pa, $V_b = -60$ V, $T_s = 250\,°C$ on steel substrates using the method of RF magnetron sputtering. Corrosion testing was performed at room temperature in a 3.5% aqueous solution of NaCl. The potentials of the samples were measured relative to the Cl–Ag electrode. The working surface area of the electrodes amounted to 1 cm^2. A platinum plate served as an auxiliary electrode. Impedance measurements were carried out at the potential of 250 mV. The corrosion current was calculated using the polarization resistance R_p by the equation [202]

$$I_{\text{cor}} = \frac{\beta_a \beta_c}{2.303 R_p (\beta_a + \beta_c)}\,, \tag{4}$$

where β_a and β_c are the anode and cathode Tafel constants, respectively.

To determine R_p, the voltage-current characteristic was measured near the corrosion potential by polarization in the cathode and anode directions. The value of R_p was calculated from the slope of the curve at the corrosion potential. An analysis of electrochemical parameters (Table 2) testifies to the effect of the modulation period of coatings on their

Table 2. Corrosion resistance test results for ZrN/CrN samples in a 3.5% aqueous solution of NaCl [85].

Parameter	Value				
	Substrate	Modulation period			
		3 μm	375 nm	200 nm	100 nm
β_a, V/decade	496.6×10^{-3}	128.1×10^{-3}	132.6×10^{-3}	323.6×10^{-3}	62.5×10^{-3}
β_c, V/decade	270.8×10^{-3}	190.6×10^{-3}	185.2×10^{-3}	540.5×10^{-3}	102.8×10^{-3}
I_{cor}, μA cm^{-2}	40.5	3.74	3.37	1.8	17.6
E_{cor}, mV	−748	−338	−339	−240	−280
V_{cor}, mm $year^{-1}$	0.3157	0.0561	0.0566	0.02347	0.02048

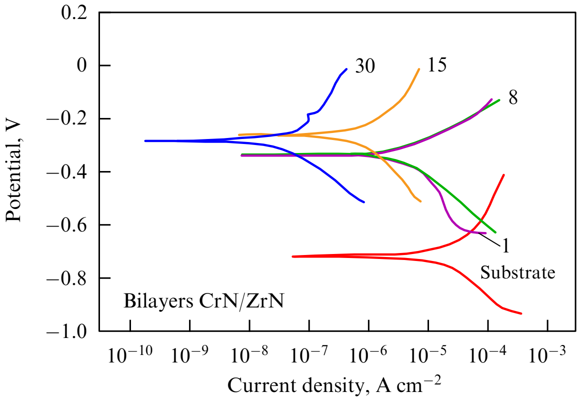

Figure 37. Tafel polarization curves of ZrN/CrN samples with the number of bilayers of 1, 8, 15, 30 [85].

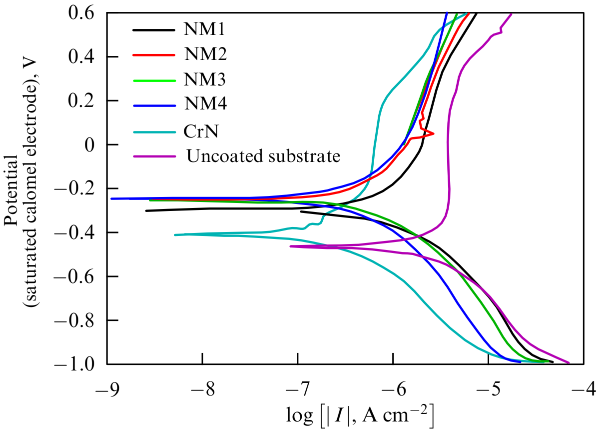

Figure 38. (Color online.) Dynamic potential polarization curves for a series of Zr/CrN coatings and a steel substrate [207].

corrosion resistance. The Tafel curves presented in Fig. 37 confirm high corrosion resistance (about 23 μm per year).

It was observed that with a decrease in the thickness of bilayers (about 100–200 nm) the corrosion attack does not affect the surface of the films. No significant changes occur in these coatings after their exposure to corrosion wear [85, 203–206]. Thus, based on the analysis of corrosion behavior of ZrN/CrN films in a 3.5% NaCl solution, the corrosion characteristics of the coatings and their interrelation with the nanometer thickness of layers in a multilayer composition were established.

In Ref. [207], the influence of layer modulation ratios in the Zr/CrN system on the structure, tribological properties, and corrosion resistance of the coating were considered. To obtain Zr/CrN condensates, the method of vacuum-arc deposition was used. The electrochemical behavior of the multilayer system was studied using the dynamic potential technique at room temperature.

Figure 38 presents polarization curves of Zr/CrN coatings, as well as an uncoated 316L steel substrate as a control sample. Based on the polarization curves, the corrosion potential values (E_{cor}) and the corrosion current density (I_{cor}) were found. Compared to the uncoated substrate, the NM(1–4) samples demonstrate higher values of E_{cor} and lower values of I_{cor}, which indicates good corrosion resistance of the coatings [208, 209].

5. Conclusion

In the presented review, a class of multilayer nanoscale coatings with a nanolayer architecture, consisting of both binary and multielement (3–6 elements) nitrides, carbides, and combinations of them, is considered. It is shown that the extremely fine-scale structural ordering at the nanometer level is a prerequisite for designing new multifunctional hard coatings. The review does not claim to be a complete analysis of numerous papers (the number of which has reached a few thousand); however, we believe that the main features manifested in these structures (systems) have already been considered, so that we can briefly mention them. Thus, the following factors were found to affect the coating properties: the size of bilayers, their interphase boundaries, the incident ion-plasma flow energy (the potential supplied to the substrate), the pulse power and duration (in the case of magnetron sputtering), the combined effect of surface energy and growth plane, the anisotropy of deformation energy, and the change in interphase boundary structures in binary multilayer nitride coatings.

As to further progress in developing multilayer coatings with alternating nanolayers of various functional purposes, a systemic approach to understanding the role of chosen materials, growth conditions, the microstructure, and the required properties is necessary. Changes in the columnar structure and grain shape, as well as in the coherence between the layers, can cause significant modification of physical-mechanical properties. Taking into account the limited applicability of the Hall–Petch relation and the fact that many hard materials integrated in multilayer films possess strong covalent bonds, the aspects related to deformation of materials (e.g., initiation of cracks, crack propagation, and a reduction in crack energy) and the fracture mechanisms should be seriously considered in theoretical modeling. Integrating new nanocrystalline, metastable, amorphous or nanocomposite layers, as well as the imposition of nanoscale gradients on the chemical composition, gradient growth of coatings, substrate temperature, or interphase design by mixing induced by a shear stress at the substrate or relaxation of stresses at layer interfaces can improve the physical-mechanical properties of multilayer thin films. Especially worth noting is the importance of studies in the field of obtaining coatings, stable at high temperatures (< 2000 °C) for protection from corrosion, since nanoscale multilayer coatings can be stable due to the predominance of the amorphous phase in the film structure.

The study was carried out with support from the Ministry of Education and Science of Ukraine, project nos 0118U003579 and 0119U100787, and was partially financed by the Center of Advanced Development, Veritas of East Kazakhstan Technical University, Oskemen, Republic of Kazakhstan.

References

1. Hazar H *Mater. Design* **31** 624 (2010)
2. Yousaf M I et al. *Surf. Coat. Technol.* **282** 94 (2015)
3. Veprek S *J. Vac. Sci. Technol. A* **31** 050822 (2013)
4. Caicedo J C et al. *Mater. Sci. Eng. B* **171** 56 (2010)
5. Eklund P et al. *Thin Solid Films* **518** 1851 (2010)
6. Kong M et al. *Appl. Surf. Sci.* **253** 4734 (2007)
7. Pogrebnjak A D et al. *Composites B* **142** 85 (2018)
8. Pu Y et al. *Appl. Surf. Sci.* **255** 2697 (2008)
9. Zhou Q et al. *J. Alloys Compd.* **698** 906 (2017)

10. Zhang S et al. *Surf. Coat. Technol.* **198** 2 (2005)
11. Musil J, Jirout M *Surf. Coat. Technol.* **201** 5148 (2007)
12. Musil J *RSC Adv.* **5** 60482 (2015)
13. Musil J, in *Thin Films and Coatings: Toughening and Toughness Characterization* (Ed. S Zhang) (Boca Raton, FL: CRC Press, Taylor and Francis Group, 2015) p. 377
14. Musil J, Vlček J, Zeman P *Adv. Appl. Ceram.* **107** 148 (2008)
15. Musil J *Surf. Coat. Technol.* **207** 50 (2012)
16. Pemmasani S P et al. *Appl. Surf. Sci.* **313** 936 (2014)
17. Wang Q, Zhou F, Yan J *Surf. Coat. Technol.* **285** 203 (2016)
18. Chen W et al. *Surf. Coat. Technol.* **265** 205 (2015)
19. Pogrebnjak A D et al. *Ceram. Int.* **43** 771 (2017)
20. Gulbiński W, Suszko T *Surf. Coat. Technol.* **201** 1469 (2006)
21. Kravchenko Ya O et al. *J. Alloys Compd.* **767** 483 (2018)
22. Shypylenko A et al. *Mater. Des.* **110** 821 (2016)
23. Bagdasaryan A A et al. *Composites B* **146** 132 (2018)
24. Barnett S A, Madan A *Scr. Mater.* **50** 739 (2004)
25. Valvoda V et al. *Thin Solid Films* **156** 53 (1988)
26. Pogrebnjak A D et al. *Phys. Usp.* **60** 586 (2017); *Usp. Fiz. Nauk* **187** 629 (2017)
27. Maksakova O V, Pogrebnjak O D, Beresnev V M *Usp. Fiz. Met.* **19** (1) 25 (2018)
28. Yao S H, Su Y L *Wear* **212** 85 (1997)
29. Pogrebnjak A D et al. *Phys. Usp.* **52** 29 (2009); *Usp. Fiz. Nauk* **179** 35 (2009)
30. Çölmekçi S, Karpuz A, Köçkar H *J. Magn. Magn. Mater.* **478** 48 (2019)
31. Pogrebnjak A D, Beresnev V M *Nanocoatings Nanosystems Nanotechnologies* (Dubai: Bentham Sci. Publ., 2013) p. 145
32. Pogrebnjak A et al. *J. Alloys Compd.* **718** 260 (2017)
33. Pogrebnjak A D et al. *ACS Appl. Mater. Interfaces* **11** 48540 (2019)
34. Holleck H, Schier V *Surf. Coat. Technol.* **76** 328 (1995)
35. Vereschaka A A et al. *Proced. CIRP* **77** 549 (2018)
36. Liu Y et al. *J. Alloys Compd.* **788** 729 (2019)
37. Wang T et al. *J. Alloys Compd.* **729** 942 (2017)
38. Carlton C E, Ferreira P J *Acta Mater.* **55** 3749 (2007)
39. Rane G K et al. *Mater. Sci. Eng. B* **243** 96 (2019)
40. Shi Y et al. *Surf. Coat. Technol.* **365** 115 (2019)
41. Balci M N, Dag S *Int. J. Solids Struct.* **161** 267 (2019)
42. Carpio P et al. *Ceram. Int.* **43** 4048 (2017)
43. Contreras E et al. *Surf. Coat. Technol.* **332** 214 (2017)
44. Kelly A, Macmillan N H *Strong Solids* (Monographs on the Physics and Chemistry of Materials) (Oxford: Clarendon Press, 1986)
45. Veprek S, Reiprich S *Thin Solid Films* **268** 64 (1995)
46. Wolf D, Lutsko J F *J. Appl. Phys.* **66** 1961 (1989)
47. Musil J, Zeman P, Baroch P, in *Comprehensive Materials Processing* Vol. 4 (Amsterdam: Elsevier, 2014) p. 325
48. Pogrebnjak A D, in *Nanomaterials-Based Coatings: Fundamentals and Applications* (Eds P N Tri, S Rtimi, C M O Plamondon) (Amsterdam: Elsevier, 2019) p. 237
49. Stueber M et al. *J. Alloys Compd.* **483** 321 (2009)
50. Walker J C et al. *Wear* **267** 965 (2009)
51. Wang H T, Xu Y X, Chen L *J. Alloys Compd.* **728** 952 (2017)
52. Veprek S et al. *Surf. Coat. Technol.* **204** 1898 (2010)
53. Qiaoling J et al. *Rare Met. Mater. Eng.* **46** 2857 (2017)
54. Nordin M, Larsson M, Hogmark S *Surf. Coat. Technol.* **106** 234 (1998)
55. Wen M et al. *Appl. Surf. Sci.* **284** 331 (2013)
56. Chen Z et al. *Acta Mater.* **168** 190 (2019)
57. Zhao Y H et al. *Int. J. Refract. Met. Hard Mater.* **32** 27 (2012)
58. Roa J J et al. *Surf. Coat. Technol.* **308** 414 (2016)
59. Carpenter J S, Misra A, Anderson P M *Acta Mater.* **60** 2625 (2012)
60. Frutos E et al. *Mater. Sci. Eng. A* **632** 137 (2015)
61. Maksakova O V et al. *J. Alloys Compd.* **831** 154808 (2020)
62. Abadias G et al. *Surf. Coat. Technol.* **202** 844 (2007)
63. Wang T et al. *J. Alloys Compd.* **729** 942 (2017)
64. Patscheider J, Zehnder T, Diserens M *Surf. Coat. Technol.* **146** 201 (2001)
65. Zhang L et al. *Surf. Coat. Technol.* **224** 120 (2013)
66. Bagdasaryan A A et al. *Mater. Lett.* **229** 364 (2018)
67. Maksakova O V et al. *Mater. Res. Express* **6** 106438 (2019)
68. Kim C et al. *Thin Solid Films* **240** 52 (1994)
69. Setoyama M et al. *Surf. Coat. Technol.* **86** 225 (1996)
70. Zhang Z, Lagally M G *Science* **276** 377 (1997)
71. Madan A et al. *Phys. Rev. Lett.* **78** 1743 (1997)
72. Wang F et al. *Acta Mater.* **127** 124 (2017)
73. Chen L, Xu Y X *Mater. Des.* **106** 1 (2016)
74. Wan H et al. *Acta Mater.* **60** 2539 (2012)
75. Harris G B *Philos. Mag. J. Sci. 7* **43** 113 (1952)
76. Lewis D B et al. *Surf. Coat. Technol.* **184** 225 (2004)
77. Pogrebnjak A D et al. *Int. J. Refract. Met. Hard Mater.* **48** 222 (2015)
78. Barshilia H C et al. *Vacuum* **85** 411 (2010)
79. Donohue L A et al. *Surf. Coat. Technol.* **94** 226 (1997)
80. Bouzakis K-D et al. *Surf. Coat. Technol.* **202** 826 (2007)
81. Baptista A et al. *Proced. Manuf.* **17** 746 (2018)
82. Pogrebnjak A D et al. *Mater. Des.* **153** 47 (2018)
83. Chen S-F et al. *Surf. Coat. Technol.* **231** 247 (2013)
84. Huang S-H et al. *Surf. Coat. Technol.* **206** 1744 (2011)
85. de Sánchez N A et al. *Adv. Mater. Res.* **38** 63 (2008)
86. Buchinger J et al. *Acta Mater.* **172** 18 (2019)
87. Skordaris G et al. *Wear* **404** 50 (2018)
88. Bobzin K et al. *Thin Solid Films* **596** 140 (2015)
89. Klimashin F F, Euchner H, Mayrhofer P H *Acta Mater.* **107** 273 (2016)
90. Gilewicz A, Warcholinski B *Surf. Coat. Technol.* **279** 126 (2015)
91. Postolnyi B O et al. *J. Alloys Compd.* **725** 1188 (2017)
92. Monshi A, Foroughi M R, Monshi M R *World J. Nano Sci. Eng.* **02** 154 (2012)
93. Raveh A et al. *Surf. Coat. Technol.* **201** 6136 (2007)
94. Veprek S, Veprek-Heijman M G J *Thin Solid Films* **522** 274 (2012)
95. Stampfl C, Freeman A J *Appl. Surf. Sci.* **258** 5638 (2012)
96. Ivashchenko V I et al. *Thin Solid Films* **564** 284 (2014)
97. Lao J et al. *Appl. Phys. Lett.* **86** 011902 (2005)
98. Ivashchenko V I et al. *Phys. Rev. B* **86** 014110 (2012)
99. Xu Y X et al. *Acta Mater.* **130** 281 (2017)
100. Wu M-K et al. *Surf. Coat. Technol.* **206** 1886 (2011)
101. Shi J et al. *J. Alloys Compd.* **727** 691 (2017)
102. Cavaleiro A J et al. *Vacuum* **139** 23 (2017)
103. Veprek S et al. *Thin Solid Films* **476** 1 (2005)
104. Lin C-H, Tsai Y-Z, Duh J-G *Thin Solid Films* **518** 7312 (2010)
105. Kim G et al. *Surf. Coat. Technol.* **200** 1669 (2005)
106. Kim M-K, Kim G-S, Lee S-Y *Met. Mater. Int.* **14** 465 (2008)
107. Li D J, Chung Y-W *Thin Solid Films* **506 – 507** 207 (2006)
108. Zhitomirsky V N et al. *Surf. Coat. Technol.* **133** 114 (2000)
109. Rizzo A et al. *Thin Solid Films* **515** 500 (2006)
110. Zhang Z G et al. *Appl. Surf. Sci.* **255** 4020 (2009)
111. Zhang J J et al. *Surf. Coat. Technol.* **201** 5186 (2007)
112. Maksakova O V et al. *J. Alloys Compd.* **776** 679 (2019)
113. Maksakova O et al. *Mater. Charact.* **140** 189 (2018)
114. Takadoum J (Ed.) *Nanomaterials and Surface Engineering* (Hoboken, NJ: John Wiley and Sons, 2013)
115. Knuyt G et al. *Thin Solid Films* **258** 159 (1995)
116. Simsek B, Ceran Ö B, Sara O N *Difficulties in Thin Film Synthesis* (Handbook of Nanomaterials and Nanocomposites for Energy and Environmental Applications, Eds O Kharissova, L Martinez, B Kharisov) (Cham: Springer Intern. Publ., 2020) p. 1
117. Musil J "Advanced hard nanocoatings: present state and trends", in *Top 5 Contributions in Molecular Sciences* (Berlin: Avid Science, 2019) p. 2
118. Anders A *Thin Solid Films* **518** 4087 (2010)
119. Thornton J A *J. Vac. Sci. Technol.* **11** 666 (1974)
120. Vook R W *Int. Met. Rev.* **27** 209 (1982)
121. Stearns D G, Mirkarimi P B, Spiller E *Thin Solid Films* **446** 37 (2004)
122. Gubicza J *Defect Structure and Properties of Nanomaterials* (Duxford: Woodhead Publ., 2017) p. 155
123. Zhang Y-M, Gu Y, Chen J-T *Eng. Anal. Bound. Elem.* **35** 708 (2011)
124. Flores M et al. *Surf. Coat. Technol.* **200** 1315 (2005)
125. Flores M et al. *Appl. Surf. Sci.* **253** 7192 (2007)
126. Benegra M et al. *Thin Solid Films* **494** 146 (2006)
127. Ma G et al. *Vacuum* **89** 244 (2013)
128. Liu K-Y, Lee J-W, Wu F-B *Surf. Coat. Technol.* **259** 123 (2014)
129. Chang Y-Y et al. *Surf. Coat. Technol.* **350** 1071 (2018)
130. Chang Y-Y et al. *Surf. Coat. Technol.* **332** 494 (2017)
131. Yang S-M et al. *Surf. Coat. Technol.* **202** 2176 (2008)
132. Deeleard T et al. *Proced. Eng.* **32** 1000 (2012)

133. Chang C-L et al. *Thin Solid Films* **516** 5324 (2008)
134. Guo C T, Lee D, Chen P C *Appl. Surf. Sci.* **254** 3130 (2008)
135. Elmkhah H et al. *J. Alloys Compd.* **688** 820 (2016)
136. Dubey P et al. *Surf. Coat. Technol.* **313** 121 (2017)
137. Gómez A G et al. *Surf. Coat. Technol.* **204** 3228 (2010)
138. Hamouda A B H, Mahjoub B, Blel S *Surf. Sci.* **661** 42 (2017)
139. Trofimov V I, Kim J, Bae S *Surf. Sci.* **601** 4465 (2007)
140. Chang Y-Y, Wu C-J *Surf. Coat. Technol.* **231** 62 (2013)
141. Wo P C et al. *Mater. Sci. Eng. A* **527** 4447 (2010)
142. Windt D L et al. *J. Appl. Phys.* **78** 2423 (1995)
143. Cerqueira M A, Torres-Giner S, Lagaron J M, in *Nanomaterials for Food Packaging* Vol. 147 (Eds M A P R Cerqueira et al.) (Amsterdam: Elsevier, 2018) p. 147
144. Adams D P *Thin Solid Films* **576** 98 (2015)
145. Windischmann H *J. Vac. Sci. Technol. A* **9** 2431 (1991)
146. Abadias G et al. *Vacuum* **100** 36 (2014)
147. Zhou X et al. *Appl. Surf.* **469** 537 (2019)
148. Depla D, Braeckman B R *Thin Solid Films* **604** 90 (2016)
149. Wadley H N G et al. *Prog. Mater. Sci.* **46** 309 (2001)
150. Reichelt K, Jiang X *Thin Solid Films* **191** 91 (1990)
151. Musil J et al. *J. Vac. Sci. Technol. A* **35** 020601 (2017)
152. Jena S et al. *J. Alloys Compd.* **771** 373 (2019)
153. Bychkov S F et al. *Solid State Ionics* **320** 297 (2018)
154. Le N M et al. *Thin Solid Films* **682** 131 (2019)
155. Zhao J P et al. *J. Phys. D* **30** 5 (1997)
156. Chekour L et al. *Surf. Coat. Technol.* **200** 241 (2005)
157. Je J H et al. *J. Appl. Phys.* **81** 6126 (1997)
158. Dong Y et al. *Appl. Phys. Lett.* **89** 121916 (2006)
159. Chang Y-Y, Wang D-Y, Hung C-Y *Surf. Coat. Technol.* **200** 1702 (2005)
160. Yashar P C, Sproul W D *Vacuum* **55** 179 (1999)
161. Zhang S et al. *Plasma Process. Polym.* **4** 219 (2007)
162. Khomenko A, Troshchenko D, Metlov L *Phys. Rev. E* **100** 022110 (2019)
163. Česáková I, Zetek M, Švarc V *Proced. Eng.* **69** 1105 (2014)
164. Rech J et al. *CIRP Ann.* **67** 65 (2018)
165. Pogrebnjak A D et al. *Protection Met. Phys. Chem. Surf.* **54** 240 (2018); *Fizikokhimiya poverkhnosti i zashchita materialov* **54** 152 (2018)
166. Khomenko A V, Lyashenko I A *Phys. Usp.* **55** 1008 (2012); *Usp. Fiz. Nauk* **182** 1081 (2012)
167. Tjong S C, Chen H *Mater. Sci. Eng. R* **45** 1 (2004)
168. Khadem M et al. *Friction* **5** 248 (2017)
169. Subramanian C, Strafford K N *Wear* **165** 85 (1993)
170. Kumar D D et al. *Surf. Interfaces* **7** 74 (2017)
171. Wang M X et al. *Surf. Rev. Lett.* **13** 173 (2006)
172. An J, Zhang Q Y *Mater. Charact.* **58** 439 (2007)
173. Ivanovskii A L *Prog. Mater. Sci.* **57** 184 (2012)
174. Presuel-Moreno F et al. *Mater. Today* **11** (10) 14 (2008)
175. Gebhard A, Haupert F, Schlarb A K, in *Tribology of Polymeric Nanocomposites. Friction and Wear of Bulk Materials and Coatings* (Tribology and Interface Engineering Series, Vol. 55, Eds K Friedrich, A K Schlarb) (Amsterdam: Elsevier, 2008) p. 439
176. Lawal J et al. *Surf. Coat. Technol.* **310** 59 (2017)
177. Yang W et al. *Acta Mater.* **122** 99 (2017)
178. Caicedo J C et al. *Appl. Surf. Sci.* **256** 5898 (2010)
179. He L, Chen L, Xu Y *Mater. Charact.* **125** 1 (2017)
180. Liu Y et al. *Scr. Mater.* **162** 33 (2019)
181. Demkowicz M J, Hoagland R G, Hirth J P *Phys. Rev. Lett.* **100** 136102 (2008)
182. Verma N et al. *Acta Mater.* **60** 3063 (2012)
183. Tilbrook M T et al. *Acta Mater.* **55** 2489 (2007)
184. Ma L W et al. *Surf. Coat. Technol.* **204** 1764 (2010)
185. Suresha S J et al. *Mater. Sci. Eng. A* **429** 252 (2006)
186. Ducros C, Benevent V, Sanchette F *Surf. Coat. Technol.* **163** 681 (2003)
187. Vanimisetti S K, Narasimhan R *Thin Solid Films* **515** 3277 (2007)
188. Cammarata R C *Scr. Metall.* **20** 479 (1986)
189. Findik F *Mater. Des.* **42** 131 (2012)
190. Anderson P M, Li C *Nanostruct. Mater.* **5** 349 (1995)
191. Koehler J S *Phys. Rev. B* **2** 547 (1970)
192. Leyland A, Matthews A *Wear* **246** 1 (2000)
193. Musil J, Zeman P *Solid State Phenom.* **127** 31 (2007)
194. Dryepondt S, Pint B A *Surf. Coat. Technol.* **205** 1195 (2010)
195. Chen H-W et al. *Surf. Coat. Technol.* **205** (Suppl. 1) S5 (2010)
196. Pogrebnyak A D et al. *Phys. Solid State* **60** 2030 (2018); *Fiz. Tverd. Tela* **60** 1986 (2018)
197. Zhang S et al. *Surf. Coat. Technol.* **214** 153 (2013)
198. He X D et al. *Surf. Coat. Technol.* **365** 65 (2019)
199. Puchi-Cabrera E S, Staia M H, Iost A *Thin Solid Films* **578** 53 (2015)
200. Iost A et al. *Thin Solid Films* **524** 229 (2012)
201. Du S et al. *Ceram. Int.* **44** 613 (2018)
202. Stern M, Geaby A L *J. Electrochem. Soc.* **104** 56 (1957)
203. Kravchenko Y O et al. *Appl. Surf. Sci.* **534** 147573 (2020)
204. Sahul, M et al. *Mater. Lett.* **276** 128180 (2020)
205. Musil J, Čerstvý R, Pogrebnjak A D *High Temp. Mater. Process. Int. Quart. High-Technol. Plasma Process.* **24** 193 (2020)
206. Pogrebnjak A D et al. *J. Superhard Mater.* **38** 393 (2016)
207. Guan X et al. *Tribol. Int.* **106** 78 (2017)
208. Pogrebnjak A D et al. *Mater. Lett.* **211** 316 (2018)
209. Grigoriev S N et al. *J. Friction Wear* **35** (5) 359 (2014)